Quantifying CH_4 point source emissions with airborne remote sensing: First results from AVIRIS-4

Sandro Meier[1,2], Marius Vögtli[2], Andreas Hueni[2], Audrey McManemin[3], Adam R. Brandt[3], Catherine Juéry[4], Vincent Blandin[5], Dominik Brunner[1], and Gerrit Kuhlmann[1]

[1]Empa, Laboratory for Air Pollution / Environmental Technology, Ueberlandstrasse 129, 8600 Duebendorf, Switzerland
[2]Department of Geography, University of Zurich, Winterthurerstrasse 190, 8057 Zurich, Switzerland
[3]Department of Energy Science & Engineering, Stanford University, United States
[4]Air Quality Laboratory, TotalEnergies, France
[5]TotalEnergies Anomalies Detection Initiatives (TADI), TotalEnergies, France

Correspondence: Sandro Meier (sandro.meier@empa.ch), Gerrit Kuhlmann (gerrit.kuhlmann@empa.ch)

Abstract. Atmospheric concentration of methane (CH_4), a ~~critical~~ potent greenhouse gas, increased significantly since pre-industrial times, with anthropogenic emissions originating primarily from agriculture, fossil fuel ~~use~~ sector and waste management. However, considerable uncertainties persist in the detection and quantification of anthropogenic CH_4 emissions. In this study, we present first CH_4 observations, plume detections and emission estimates from the new state-of-the-art Airborne Visible InfraRed Imaging Spectrometer 4 (AVIRIS-4), which participated in a blind controlled release experiment in September 2024 in southern France. We used an albedo-corrected matched filter to retrieve CH_4 maps from the spectral images and estimated CH_4 emission with the Integrated Mass Enhancement (IME) and Cross-Sectional Flux (CSF) methods. Our results demonstrate that AVIRIS-4 can reliably detect emissions as low as $5.5 \, \mathrm{kg \, CH_4 \, h^{-1}}$ under good weather conditions at low flight altitudes ($<1500 \, \mathrm{m}$) and $1.45 \, \mathrm{kg \, CH_4 \, h^{-1}}$ under ideal conditions. These low-altitude detection limits are substantially lower than published detection limits for the predecessor instrument AVIRIS-NG, which were in the order of 10 - 16 $\mathrm{kg \, CH_4 \, h^{-1}}$ under comparable conditions. While AVIRIS-4 provides highly accurate CH_4 maps at $<0.5 \, \mathrm{m}$ resolution, emission estimation is limited by the accuracy of the effective wind speed, whose uncertainty and natural variability contribute substantially to the overall uncertainty. Using wind speed at source height performs well for small releases (below $20 \, \mathrm{kg \, CH_4 \, h^{-1}}$) (rRMSE = 1.065; rMBE = 0.361) and overall (rRMSE = 0.702; rMBE = -0.204). Using literature-derived effective wind speeds improves the apparent fit between estimated and reported CH_4 emissions, but degrades performance both in overall agreement (rRMSE = 2.098; rMBE = 0.964) and for low-emission events (rRMSE = 2.367; rMBE = 1.711). Interestingly, the high spatial resolution makes it possible to retrieve the cast shadow of the CH_4 plume, which can be used to estimate source and plume height, and could provide an approach for better constraining the height-dependency of the effective wind speed. On the bottom line, the controlled release experiment provides critical insights into the sensor's capabilities and guides further improvements to detect and quantify low intensity sources in the fossil fuel and waste management sectors, with implications for more accurate global greenhouse gas monitoring.

1 Introduction

Methane (CH_4), a potent greenhouse gas with a global warming potential 28 times higher than CO_2 on a timescale of 100 years, has seen an almost threefold rise from 700 ppb pre-industrial levels to over 1900 ppb due to natural and anthropogenic sources (Seinfeld and Pandis, 2016). Major contributors include agriculture, fossil fuels, and waste. Due to its short lifetime of only 9 years, CH_4 is removed more quickly compared to most other greenhouse gases. Reducing CH_4 emissions is therefore considered an effective measure to mitigate anthropogenic climate change in the near term. However, there are still significant uncertainties in the quantification of anthropogenic CH_4 emissions (Saunois et al., 2020).

For instance, Saunois et al. (2020) estimated that uncertainties in emissions from the fossil fuel sector are around 20-35% with strong regional variations. Reducing these uncertainties is challenging for several reasons. One of them is the fact that an important fraction of anthropogenic CH_4 emissions, e.g., from the fossil fuel sector, result from unintentional leakage, which cannot be accurately quantified. Additionally, global CH_4 emission estimates depend on a network of monitoring stations, which is dense and accurate in northern and mid-latitudes but sparser in other regions (Saunois et al., 2020). For these reasons, satellite remote sensing observations of CH_4 have been used to estimate the emissions in a top-down approach (e.g. Alexe et al., 2015; Bousquet et al., 2018; Fraser et al., 2013). These remote sensors can be separated into area flux mappers (e.g. Sentinel-5P, MethaneSAT ~~, GOSAT-GW and CO2M~~and GOSAT-GW) which are designed to have a global to regional coverage and point flux mappers (e.g. Landsat-8, Sentinel-2, GHGSat, PRISMA and EnMAP) which are used to observe regional to local emissions (Jacob et al., 2022).

Most of the currently available CH_4 imagers are limited by spatial and/or spectral resolution which hinders the precision and accuracy of the emission estimates (Bousquet et al., 2018). This results in high detection limits in the range of a few 100 to several 1000 $\mathrm{kg\,CH_4\,h^{-1}}$ for spaceborne instruments such as Sentinel-2 and Sentinel-5, PRISMA, EnMAP or GHGSat (e.g. Jacob et al., 2022; Gorroño et al., 2023; Joyce et al., 2023). For airborne instruments with a higher spatial resolution such as MethaneAIR, GHGSat-AV and the Airborne Visible InfraRed Imaging Spectrometer - Next Generation (AVIRIS-NG), the detection limit decreases to 10 to 100 $\mathrm{kg\,CH_4\,h^{-1}}$ under favourable conditions (e.g. Cusworth et al., 2021; Duren et al., 2019; Jongaramrungruang et al., 2022; Kuhlmann et al., 2025; Guanter et al., 2025).

CH_4 emissions from sources with small emission strengths that cannot be quantified from space ($\lesssim 100$ $\mathrm{kg\,CH_4\,h^{-1}}$) are crucial for two reasons: First, leakages from the production and use of fossil fuels are often small and remain undetected by satellite-based approaches. Second, CH_4 emissions from oil and gas production have a lognormal distribution with many small sources but only a few large ones (e.g. Balcombe et al., 2018; Stavropoulou et al., 2023; Williams et al., 2025). Accurate knowledge of the emission distribution of sources from a given sector or country is crucial for extrapolating CH_4 emissions from the entire sector or country by accounting for sources below the detection limit (Zavala-Araiza et al., 2015; Zhang et al., 2023; Kuhlmann et al., 2025).

The detection of low intensity CH_4 sources requires a sensor that combines high spatial resolution with a good signal-to-noise ratio. One such state-of-the-art sensor is the new Airborne Visible InfraRed Imaging Spectrometer 4 (AVIRIS-4). It was developed by NASA JPL as a successor of AVIRIS-NG in parallel to its sister instruments Earth Surface Mineral Dust Source

Investigation (EMIT) and AVIRIS-3 which are in service on board the ISS and as airborne sensor respectively (Hueni et al., 2025). In comparison with its predecessor, AVIRIS-4 has traded some of its spectral resolution in order to enhance its spatial resolution and SNR (see Table 1). In this paper, we present the processing chain for retrieving CH_4 emissions from AVIRIS-4 measurements, show CH_4 maps and emission estimates from a blind controlled release experiment and characterise the

60   capabilities and limitations of AVIRIS-4 for CH_4 emission quantification. The analysis considers the influence of flight altitude, meteorological conditions such as wind speeds and atmospheric stability, illumination and viewing conditions, and surface reflectance on the detection limit and the quality of the emission quantifications, providing guidance for future campaigns.

2   Data and Methods

This section covers the description of AVIRIS-4 (Section 2.1) used for the acquisition of remote sensing data in the controlled

65   release experiment (Section 2.2) and the data processing chain from radiance data processing (Section 2.3), CH_4 retrieval (Section 2.4) and CH_4 emission estimation (Section 2.5) to the estimation of uncertainties (Section 2.6).

2.1   AVIRIS-4 sensor specification

AVIRIS-4 is a state-of-the-art imaging spectrometer with identical core components as NASA JPL's AVIRIS-3 and the EMIT spectrometer (Green et al., 2022; Shaw et al., 2022; Hueni et al., 2025). The spectrometer is equipped with a 1280-pixel

70   sensor array and records hyperspectral data in 328 bands spanning the ultraviolet (UV) to the shortwave infrared (SWIR). In practice, 1241 pixels receive sufficient illumination and SNR, and 287 bands are retained for data processing. Detailed sensor specifications are provided in Hueni et al. (2025). Compared to its predecessor it offers enhanced stability, spatial sampling interval (hereafter referred to as spatial resolution) and signal-to-noise ratio (SNR) (see Table 1).

2.2   Controlled release experiment

75   The data for this analysis was acquired during a single-blind controlled release experiment organised by the Environmental Assessment and Optimization Group at Stanford University between the 16th and 20th of September 2024 at the TotalEnergies Anomalies Detection Initiatives (TADI) site in Lacq in the south of France (latitude: 43.412°, longitude: -0.63643 0.636°, elevation a.m.s.l.: 95 m) (see Figure 1a). A total of 13 commercial and academic teams, using a range of technologies - including continuous monitoring, vehicle-based measurements, drones, airborne in-situ measurements, remote sensing from aircraft, and

80   satellites - participated in the experiment. The results of all teams were collected and analysed in McManemin (2025). On each campaign day (8:00 - 18:00 CEST), up to 9 individual controlled releases with rates varying between 0.02 and 350 $\mathrm{kg\,CH_4\,h^{-1}}$ were conducted at different unknown heights between 0.01 to 6.5 m above ground and at different unknown locations on the study site (see Figure 1b). Each release lasted for 45 minutes and was followed by a 15 minute break before the start of the next release. In some periods, no CH_4 was released to enable the detection of false positives. Additionally, the wind speed was

85   measured using a ZX 300 Doppler wind lidar positioned 100 m from the emission sources. The instrument recorded horizontal and vertical wind speeds, as well as wind direction, at preselected heights between 10 and 300 m above ground level, with a

Table 1. Specifications of AVIRIS-4 compared to AVIRIS-NG, adapted from Green et al. (2022) and Hueni et al. (2025).

Category	AVIRIS-4	AVIRIS-NG
SPECTRAL		
Range	375 to 2504 nm	380 to 2510 nm
Sampling	7.4 nm	5 nm
Response (FWHM)	1 to 1.5 × sampling	1 to 1.5 × sampling
Calibration	±0.1 nm	±0.1 nm
RADIOMETRIC		
Range	0 to max Lambertian	0 to max Lambertian
Signal-to-noise ratio (SNR)	>3000 @ 600 nm	>2000 @ 600 nm
	>1200 @ 2200 nm	>1000 @ 2200 nm
Calibration	97% (<3% uncertainty)	95% (<5% uncertainty)
SPATIAL		
Swath samples	1241	600
Swath angle	40.2° field-of-view	34° field-of-view
IFOV	0.6 mrad	1 mrad
FPS	213	10 - 100
Response (FWHM)	1 to 1.5 × sampling	1 to 1.5 × sampling

temporal resolution of approximately 20 seconds. Participating teams were aware of the timing of releases while locations and flow rates of the releases as well as the wind data were only made available after all teams had submitted their initial emission estimates. Details of the release experiment, the participating teams and the synthesis can be found in McManemin (2025). For the campaign, AVIRIS-4 was mounted on a hydraulic stabilisation mount and built into a Cessna 208B Grand Caravan EX. The aircraft flew over the release site in either north-south or east-west direction at different altitudes of 12000, 9000, 6000, 4200 and 3300 ft or 3660, 2740, 1830, 1280, 1000 m above mean sea level (~~amsl~~a.m.s.l.) (see Figure 1a). This resulted in average spatial resolutions of 2.0, 1.5, 1.0, 0.7 and 0.5 m ~~across~~ across-track and 0.35 m ~~along~~along-track. For the remainder of the article, all wind speed heights are given in metres above ground level and all flight altitudes in feet ~~above mean sea level.~~a.m.s.l.

2.3 Data processing

2.3.1 Radiometric and spectral calibration, georeferencing

The level 0 data acquired by AVIRIS-4 consists of raw digital numbers ~~and has the spatial dimensions~~ organized into along-track and ~~across-track as well as~~ across-track spatial dimensions and a spectral dimension. The level 0 data was converted
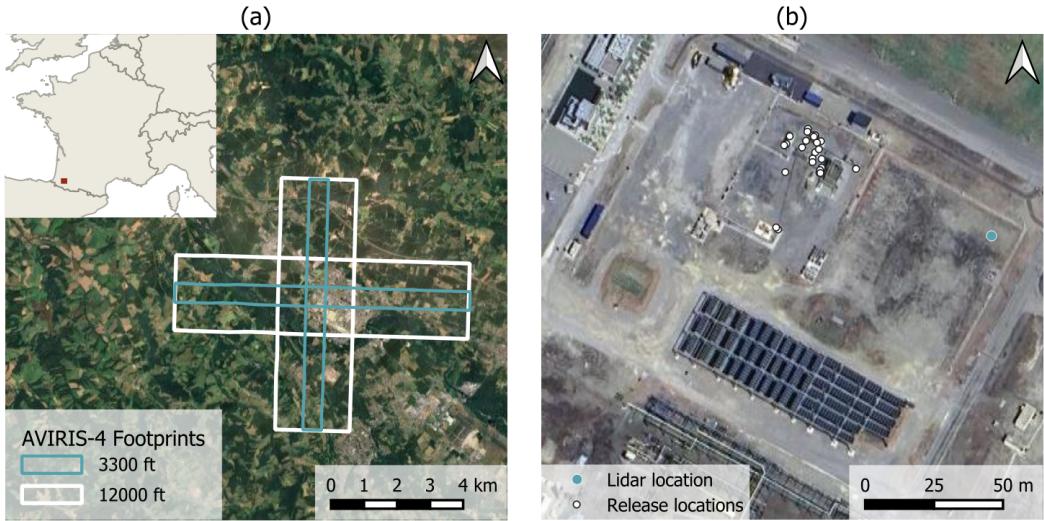
Figure 1. (a) Location of the controlled release experiment at the TADI site in the south of France (red polygon in the inset map). Superimposed are the imaging footprints of AVIRIS-4 for overpasses at 3300 and 12000 ft. (b) Aerial view of the site with the locations of the wind lidar as well as the potential release locations. The background maps are obtained from © Google Earth.

into level 1 at-sensor radiances (in $\mu\mathrm{W\,cm^{-2}\,nm^{-1}\,sr^{-1}}$) using laboratory-measured calibration coefficients. The level 1 data was georeferenced using a parametric approach (Schläpfer and Richter, 2002), where the geometry of the sensor, its location and orientation acquired from ~~GNSS~~ global navigation satellite system (GNSS) and inertial navigation system (INS) data were combined with a digital elevation model (IGN, 2018) to project the radiometrically corrected data onto the surface with sub-pixel accuracy. Details on the processing are described in Hueni et al. (2025).

2.3.2 Masking of shadows and water surfaces

~~Dark~~ Observations over dark surfaces such as cast shadows and water bodies have a low SNR and therefore produce artefacts when processing the data. Additionally, cast shadows only contain diffuse radiance, which is inconsistent with the non-scattering assumption in CH_4 retrieval. Cast shadows were especially pronounced in our data, as the controlled release experiment took place in late September under low solar zenith angles (SZA). For this reason, we masked these areas using a modified version of the cast detection method described in Schläpfer et al. (2018), using radiances at 450 nm for blue (L_b), 670 nm for red (L_r) and 780 nm for near-infrared (NIR) (L_n):

$$i_{sh} = \frac{L_r + k_n(L_n - L_r)_{>0}}{L_b} \cdot \frac{1}{a\,e^{b\,L_{b,\text{dark}}}}. \tag{1}$$

We used the default parameters $k_n = 0.1$, $a = 1.58$ and $b = -0.04$ from Schläpfer et al. (2018). Next, we divided the inverse of the resulting index by the integrated radiance over all wavelengths. After empirical evaluation, values larger than 0.25 were masked prior to applying the matched filter.

2.4 CH$_4$ retrieval

We retrieved CH$_4$ maps from the AVIRIS-4 radiance ~~cube~~ cubes using the computationally efficient matched filter approach following Foote et al. (2020) and further refined by Kuhlmann et al. (2025). The filter detects a known signal within a noisy background by enhancing the signal relative to the noise, effectively maximising the output signal-to-noise ratio under the assumption of additive Gaussian noise.

2.4.1 Matched filter

Using a linearised form of the Beer-Lambert law, the matched filter (MF) takes the form

$$\alpha_\epsilon = \frac{(L_{\text{obs}} - \hat{\mu}) \cdot \hat{S}^{-1} \cdot t}{t^\top \cdot \hat{S}^{-1} \cdot t} \tag{2}$$

where α_ϵ represents the CH$_4$ column enhancement, L_{obs} the observed spectrum in the two wavelength ranges 1480 to 1800 and 2080 to 2500 nm, $\hat{\mu}$ and $\hat{S}$ the median and covariance of the observed spectrum and $t = \hat{\mu} \cdot -s$ the target spectrum. We used the negative of the unit absorption spectrum of CH$_4$ s to align Eq. 2 with derivations in other studies. Thereby, s is calculated using the radiative transfer equation assuming a geometric air mass factor (AMF), no atmospheric scattering according to Kuhlmann et al. (2025) and a CH$_4$ enhancement ϵ in the lowest ~~1000-m~~ 1000 m layer respectively. The calculation of the plume-specific enhancement was achieved through an iterative approach, wherein the CH$_4$ maps were initially derived under the assumption of an enhancement of 0.01 ppm. The mean enhancement in the detected plume was then used for the subsequent iteration of the matched filter, which converged after ~~two to three iterations .~~ three iterations with changes between successive iterations falling below a 5% threshold. Our iterative approach reduces the approximation error introduced by the linearisation of the Beer-Lambert law by expanding around the current estimate of α rather than $\alpha = 0$, which decreases the linearisation error quadratically in the update step. For large enhancements, this substantially mitigates non-linear absorption effects.

2.4.2 Lognormal matched filter

Due to the linearisation of the Beer-Lambert law used in the derivation of ~~the matched filter , it is~~ most matched filter approaches, they are only valid for weak CH$_4$ enhancements. Therefore, Schaum (2021) argued that a lognormal matched filter (LMF) provides the uniform most powerful solution for the detection of trace gas plumes, which takes the following form:

$$\alpha_\epsilon = \frac{(\ln(L_{\text{obs}}) - \hat{\mu}) \cdot \hat{\mathbf{S}}^{-1} \cdot \mathbf{s}}{\mathbf{s}^\top \cdot \hat{\mathbf{S}}^{-1} \cdot \mathbf{s}} \tag{3}$$

where $\mathbf{s}$ is the same unit absorption spectrum as above. This approach has been implemented and evaluated by Pei et al. (2023) for synthetic WRF-LES and observed data from the PRISMA satellite. According to Schaum (2021), the LMF could improve the detection performance for pixels with attenuated signal, e.g. with weak enhancement or at higher flight altitudes, due to the more realistic mean spectrum $\hat{\mu}$ in logarithmic space. In the present study, we evaluated the LMF only exploratively to illustrate its behaviour on AVIRIS-4 data with an emphasis on the smallest and largest release events.

2.4.3 Albedo correction

We applied the matched filter to the at-sensor radiance of each across-track position to avoid striping caused by differences in radiometric and spectral calibration of the sensor pixels. However, as outlined in Fahlen et al. (2024), the assumption that the reference solar spectrum L_0 can be approximated by the mean spectrum $\hat{\mu}$ introduces a bias in the CH_4 column enhancement α_ϵ over heterogeneous surfaces, which must be corrected as follows:

$$\alpha_{corr} = \frac{1}{R} * \alpha_\epsilon \quad \text{with} \quad R = \frac{(L_{\text{obs}} * -s) \cdot \hat{S}^{-1} \cdot t}{t^\top \cdot \hat{S}^{-1} \cdot t} \tag{4}$$

While the correction factor helps mitigate biases in CH_4 enhancements, it also amplifies retrieval noise for dark surfaces with a low signal-to-noise ratio. This effect could be mitigated by masking cast shadows and water surfaces before applying the matched filter.

2.4.4 Plume shadow correction

In some of the AVIRIS-4 observations, we observed double plumes due to plume shadows (see Sect. 3.5.4). They present a challenge for emission estimation because the CH_4 retrieval assumes that the light traverses the plume twice, assuming a geometric AMF that depends both on the solar zenith angle (SZA) and viewing zenith angle (VZA):

$$\text{AMF}_{\text{geom}} = \sec(\text{SZA}) + \sec(\text{VZA}) \tag{5}$$

At the source location, however, the signal originating from the plume does not pass through the plume a second time after ground reflection, and thus it is independent of the VZA. Consequently, CH_4 enhancements should be scaled by c_{plume}:

$$c_{\text{plume}} = \frac{\text{AMF}_{\text{geom}}}{\sec(\text{VZA})} \tag{6}$$

For the plume shadow enhancement, the respective correction factor is given by

$$c_{\text{shadow}} = \frac{\text{AMF}_{\text{geom}}}{\sec(\text{SZA})} \tag{7}$$

When the plume and its shadow were clearly resolved, we estimated the emissions and applied the corresponding correction factor. However, when the plumes partially overlapped, this separation was not feasible, limiting the applicability of the correction method. In such situations, we employed the integrated mass enhancement (IME), which aggregates all detected pixels without explicitly distinguishing between the plume and its shadow.

2.5 CH_4 emission estimation

To estimate the CH_4 emissions, we used the integrated mass enhancement (IME) and cross-sectional flux (CSF) method implemented in the Python library for data-driven emission quantification (*ddeq*) (Kuhlmann et al., 2024). ~~The CSF performs better~~ We used the CSF for longer plumes and more turbulent conditions as it averages the fluxes along several cross-sections. Conversely, the IME ~~is more appropriate~~ was used for short plumes and plumes that deviate from a Gaussian plume shape such

as for overlapping double plumes. Both methods assume steady-state conditions of wind speed and emission rate. Limits of this assumption are further discussed in Section 4.2.

All mass-balance based methods require an estimate of the wind speed U. Ideally, U would correspond to the effective wind speed U_{eff}, which is the mean speed at which the plume is transported (Kuhlmann et al., 2024). However, as the vertical CH_4 profile is unknown, we used four different approaches to obtain a wind speed estimate:

1. 10 m wind speeds U_{10} from ERA5 reanalysis data (Hersbach et al., 2018) as used for the initial reporting in McManemin (2025) as ground-based lidar measurements were not available prior to unblinding.

2. 10 m wind speeds U_{10} from wind lidar measurements.

3. A linear scaling of the 10-m wind speed derived from model simulations for GHGSat (Varon et al., 2018) :

$$U_{\text{eff}} = 1.47 \cdot U_{10} \tag{8}$$

4. Wind speed at source height U_s, assuming a logarithmic wind profile (Fleagle and Businger, 1980; Seinfeld and Pandis, 2016). Wind profiles were derived assuming a surface roughness of 0.1 m and using on-site measurements of temperature and wind speed, combined with sensible heat fluxes from ERA5 reanalysis data (Hersbach et al., 2018). While plume rise and vertical mixing were not explicitly incorporated into the wind speed calculations, their potential influence was accounted for in the uncertainty analysis.

We also conducted a sensitivity analysis using lidar wind speeds at other elevations above ground level.

2.5.1 Integrated mass enhancement

The IME approach derives the emission rate Q based on the integrated mass enhancement M of a plume and a residence time τ during which CH_4 resides within the detectable plume. This residence time is approximated by the wind speed U and the length L of the detectable plume (Kuhlmann et al., 2024).

$$Q = \tau \cdot M = \frac{U}{L} \cdot M \tag{9}$$

The plume length L was calculated as the arc length of the centre line curve fitted to the detected plume.

The integrated mass M was computed as

$$M = \sum_{(i,j) \in \mathcal{P}_a}^{n} (V_{i,j} - V_{\text{bg}}) \cdot A_{i,j} \tag{10}$$

where $V_{i,j}$ is the vertical column density, V_{bg} is the background vertical column density, and $A_{i,j}$ is the pixel area. The trace gas mass was summed up over the n pixels of the integration area $\mathcal{P}_a$ which was obtained by a sufficient extension of the detected plume in the crosswind direction to include pixels with enhancements below the detection limit. A local CH_4 background V_{bg} was calculated by applying a low-pass Gaussian filter to the CH_4 maps after masking the enhancements including a buffer (Kuhlmann et al., 2024).

2.5.2 Cross-sectional flux method

For the CSF, the detected plume is divided into multiple polygons. As in Kuhlmann et al. (2024), a Gaussian curve with linear background trend was then fitted to the CH$_4$ enhancements of each polygon to obtain the line densities q:

$$g(y) = \frac{q}{\sqrt{2\pi}\sigma} \exp\left(-\frac{(y-\mu)^2}{2\sigma^2}\right) + my + b \tag{11}$$

Here, y is the across-plume direction, σ to the standard width and μ to the mean of the fitted Gaussian curve with linearly changing background with slope m and offset b.

The emissions Q were then calculated as the product of the wind speed U and the uncertainty-weighted mean of all line densities $\bar{q}$:

$$Q = U \cdot \bar{q} \tag{12}$$

2.6 Estimation of uncertainty

Below we describe how uncertainty components are estimated and propagated for each input to the emission quantification.

2.6.1 CH$_4$ Columns

The uncertainty of CH$_4$ columns σ_V was calculated as

$$\sigma_V = \sqrt{\sigma_t^2 + \sigma_{\text{inst}}^2}\sqrt{\sigma_t^2 + \sigma_{\text{CH}_4}^2} \tag{13}$$

where σ_{inst} accounts for correlated and uncorrelated radiance-dependent instrument uncertainties. For this analysis, it was calculated using the EMIT noise model and propagated through the MF according to Fahlen et al. (2024). For future analyses, a noise model for AVIRIS-4 will be used, which is currently under development. σ_{CH_4} is the standard deviation of retrieved CH$_4$ columns in a plume-free region next to the release location with similar surface properties. σ_t represents correlated uncertainties in the target t due to no-scatter assumptions for the calculation of the unit absorption spectrum s, which was estimated at a conservative 5% for this campaign based on Kuhlmann et al. (2025).

2.6.2 Pixel area

Uncertainty in pixel area (σ_A) is treated as a systematic spatial uncertainty, reflecting geolocation and georectification errors. During this campaign, geolocation accuracy was reduced due to a faulty cable, which impaired the temporal synchronization between GNSS data and AVIRIS-4 measurements. To assess the resulting geolocation uncertainty, AVIRIS-4 imagery was visually compared with Google Earth reference imagery. Based on this comparison, a conservative uncertainty of 5% of the nominal pixel area was assumed. The cable issue has since been resolved, and additional measures have been implemented to prevent similar problems in future campaigns.

2.6.3 Wind speed

The uncertainty of the on-site measured wind speed σ_U is assumed to consist of four terms:

$$\sigma_U = \sqrt{\sigma_{\text{inst}}^2 + \sigma_{\text{rep}}^2 + \sigma_{\text{eff}}^2 + \sigma_{\text{var}}^2} \tag{14}$$

The term σ_{inst} represents the systematic measurement uncertainty of the wind lidar which was estimated as 5% of the wind speed, based on guidance from the site operators. The term σ_{rep} represents the error associated with the spatial displacement between the wind lidar and the actual plume locations. Given the close proximity of the lidar to the source positions in this study, this component is assumed to be negligible or already captured in σ_{var} (see below). The term σ_{eff} reflects the uncertainty introduced by the use of the wind speed at source height instead of a concentration weighted wind profile. It was quantified by calculating the mean relative difference between the wind speed at source height and a Gaussian-weighted logarithmic wind profile. For the latter, we weighted the logarithmic wind profile with Gaussian curves around the source height with standard deviations ranging from 0.1 to 5 m and source heights between 0.01 and 6.5 m as experienced during the controlled release experiment. σ_{eff} was found to be in the order of 30% for sources between 0 and 1.5 m above the ground and less than 5% for sources which are more elevated. Here, we used an estimate of 15%. Finally, σ_{var} represents the uncorrelated errors due to the natural variability of on-site measured wind data during the overpass. It was quantified as the standard deviation of U_{10} over a one-minute window, consistent with the typical residence time of most detectable plumes, which was estimated to be no more than one minute.

2.6.4 IME

The uncertainties of the emission estimates σ_Q of the IME were determined by the propagation of error:

$$\sigma_Q = Q \cdot \sqrt{\left(\frac{\sigma_U}{U}\right)^2 + \left(\frac{\sigma_L}{L}\right)^2 + \left(\frac{\sigma_M}{M}\right)^2} \tag{15}$$

The uncertainty of the plume length σ_L was estimated as 10% of the plume length or at least half of a pixel. The uncertainty of the integrated mass σ_M was calculated as

$$\sigma_M = \sqrt{\sum_{(i,j)\in\mathcal{P}_a}^{n} \left[(A_{i,j} \cdot \sigma_{V_{i,j}})^2 + (A_{i,j} \cdot \sigma_{V_{\text{bg}}})^2 + \left((V_{i,j} - V_{\text{bg}}) \cdot \sigma_{A_{i,j}}\right)^2 \right]} \tag{16}$$

where $\sigma_{V_{i,j}}$ corresponds to the pixel-wise uncertainty of the vertical column density V. Using the trace gas column enhancement $V_{\text{enh}_{i,j}} = V_{i,j} - V_{\text{bg}}$, Eq. 16 simplifies to

$$\sigma_{\text{enh}} = \sqrt{\sum_{(i,j)\in\mathcal{P}_a}^{n} \left[(A_{i,j} \cdot \sigma_{V_{\text{enh}_{i,j}}})^2 + (V_{\text{enh}_{i,j}} \cdot \sigma_{A_{i,j}})^2 \right]} \tag{17}$$

where $\sigma_{A_{i,j}} = \sigma_{\bar{A}}$ and $\sigma_{V_{\text{enh}_{i,j}}} = \sigma_{V_{\text{enh}}^-}$ were assumed to be constant and correspond to the mean within the plume.

2.6.5 CSF

The uncertainties of the emission estimates σ_Q of the CSF were determined as

$$\sigma_Q = \sqrt{\bar{q}^2 \cdot \sigma_U^2 + U^2 \cdot \sigma_{\bar{q}}^2} \tag{18}$$

The uncertainty of the mean line densities $\sigma_{\bar{q}}$ was obtained as the uncertainty of the mean of the fitted fluxes q along the plume, which accounts for uncertainties σ_q of the individual cross sections. Since $\sigma_{\bar{q}}$ decreases with the square root of the number of line densities and does not account for the correlation of consecutive line densities, this uncertainty is set to at least 10% of the mean line density:

$$\sigma_{\bar{q}} = \min(\sigma_{\bar{q}}, 0.1 \cdot \bar{q}) \tag{19}$$

The uncertainty of each cross-section σ_q was calculated from the uncertainty of the Gaussian fit to each sub-polygon σ_{gauss} and the mean uncertainty of the pixel area $\sigma_{\bar{A}}$ within a sub-polygon:

$$\sigma_q = \sqrt{\sigma_{\text{gauss}}^2 + \left(\frac{q}{\bar{A}} \cdot \sigma_{\bar{A}}\right)^2} \tag{20}$$

2.7 ~~Probability of detection~~

~~We computed the probability of detection (POD) for AVIRIS-4 according to Conrad et al. (2023) as a function of reported emissions Q_{rep}, U_{10} and flight altitude $\tilde{h}$ using the flags "detected" and "not detected" by optimising the predictor and inverse link functions. This resulted in the following POD function:~~

$$\text{POD} = 1 - \left(1 + \left(1.03 \times 10^{10}\right) \frac{\left(5.18 \times 10^8\right) Q^{1.93}}{\left(\dfrac{\tilde{h}}{1000}\right)^{3.88} (u_{10} + 97.0)^{9.97}}\right)^{-1.84}$$

3 Results

In what follows, we summarise the observing conditions relevant to CH_4 retrievals during the controlled-release experiment (Section 3.1). We then present representative plume images from multiple releases across varied conditions (Section 3.2). Next, we assess how key parameters influence retrieval performance (Section 3.5), derive detection limits (Section 3.3), and compare estimated emissions with reported values (Section 3.4).

3.1 Controlled release experiment

In contrast to previous efforts, this new generation of controlled release experiments was planned to reflect more realistic natural conditions. While this allows to assess sensor performance in diverse terrain and meteorological conditions it also

280 introduce introduces limitations associated to different surface coverage, cast shadows and cloud conditions (see Figure 2 for detailed meteorological setting during all experiments, and Figures A3, A4, A5 and A6 in the Appendix for wind information). Despite these challenges, we were able to fly 100 overpasses at different hours of the day (see Figure 3a) and at five altitudes (see Figure 3b), which allowed us to evaluate the influence of wind speeds and spatial resolution on the CH_4 detection and emission estimation. Flights at all flight levels were only scheduled for the first release in the morning and afternoon after
285 refuelling. The atmospheric stability was estimated to be neutral to unstable for all observations based on the Pasquill stability classes using U_{10}.

Cloud cover
○: clear, ◔: few, ◑: scattered, ◕: broken, ●: overcast

Local time [UTC+2]	16.09.2024	17.09.2024	18.09.2024	19.09.2024	20.09.2024	SZA [°]
09:00	○	n=0 ●	n=0 ●	n=0 ●	n=0 ●	
10:00	○	n=0 ●	n=0 ●	n=0 ●	n=0 ●	
11:00	**n=5** ○	n=0 ●	**n=7** ◔	n=0 ●	n=0 ●	
12:00	n=8 ○	n=8 ◑	n=8 ○	n=0 ●	n=0 ●	
13:00	n=8 ○	n=1 ◕	**n=7** ○	n=0 ●	n=0 ●	
14:00	n=0 ○	n=0 ◕	n=4 ○	n=0 ◕	n=0 ●	
15:00	n=7 ◔	n=0 ◕	n=0 ◔	n=8 ◑	n=0 ●	
16:00	**n=8** ◔	n=0 ◕	n=8 ◑	n=8 ◔	n=0 ●	
17:00	◔	●	n=2 ◕	n=8 ○	●	
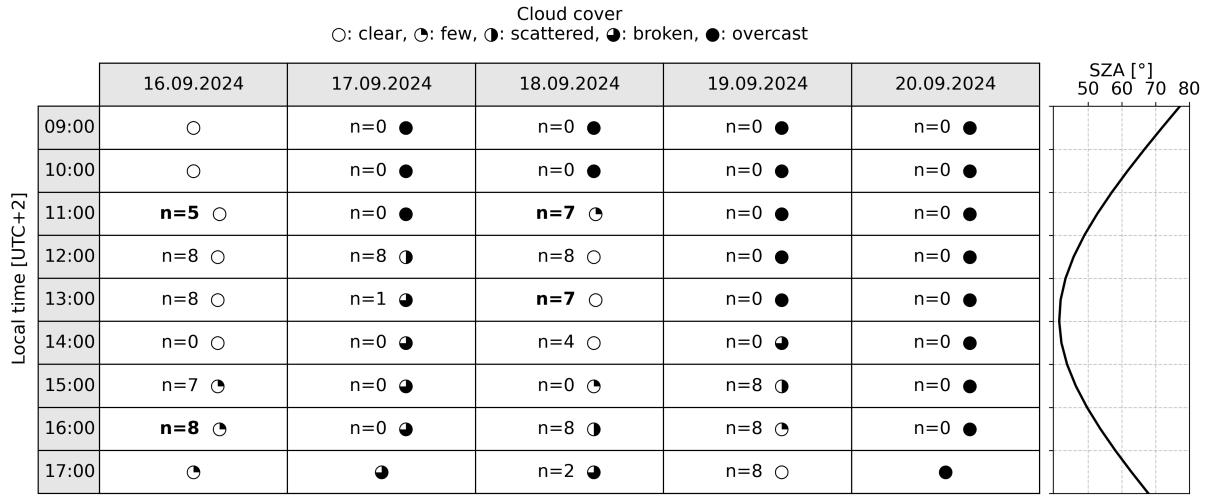
Figure 2. Schedule of the controlled release experiment with the number of overpasses n for each release and a symbol for the average cloud conditions during the release. As the releases started either at '00, '30 or '45, the row label indicates the hour of the release end in local time. If no number of overpasses is given, no release took place during that time window. Bold entries indicate releases observed at all altitude levels; otherwise, observations were limited to 4200 and 3300 ft. The right-hand panel shows the average SZA for each hour.

3.2 Examples of plume images

Figure 4 (upper row) presents three optimal examples of plumes resulting from three different releases. The plumes appear largely linear, with minimal influence from turbulence, which is favourable for emission estimation. For stronger sources,
290 retrieval noise is barely noticeable, but at lower intensities - such as the 26.4 $\mathrm{kg\,CH_4\,h^{-1}}$ release - it can interfere with the plume signal and hinder accurate attribution of enhanced pixels (see Section 3.5.5).

The lower row in Figure 4 shows three turbulent plumes observed during overpasses at 4200 ft, where local enhancements caused by turbulent eddies are clearly visible. In these cases, the CSF method outperforms the IME approach, as the effect of turbulence is reduced through averaging across multiple cross-sections.
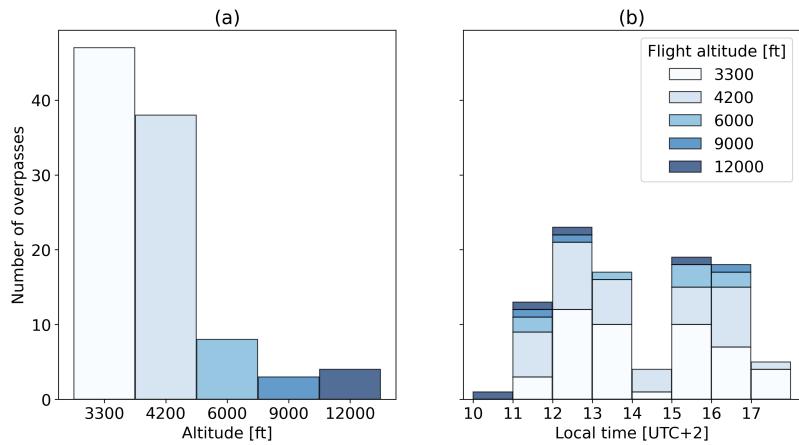
Figure 3. (a) Number of overpasses at five different altitudes above mean sea level. (b) Number of overpasses at different hours of the day.
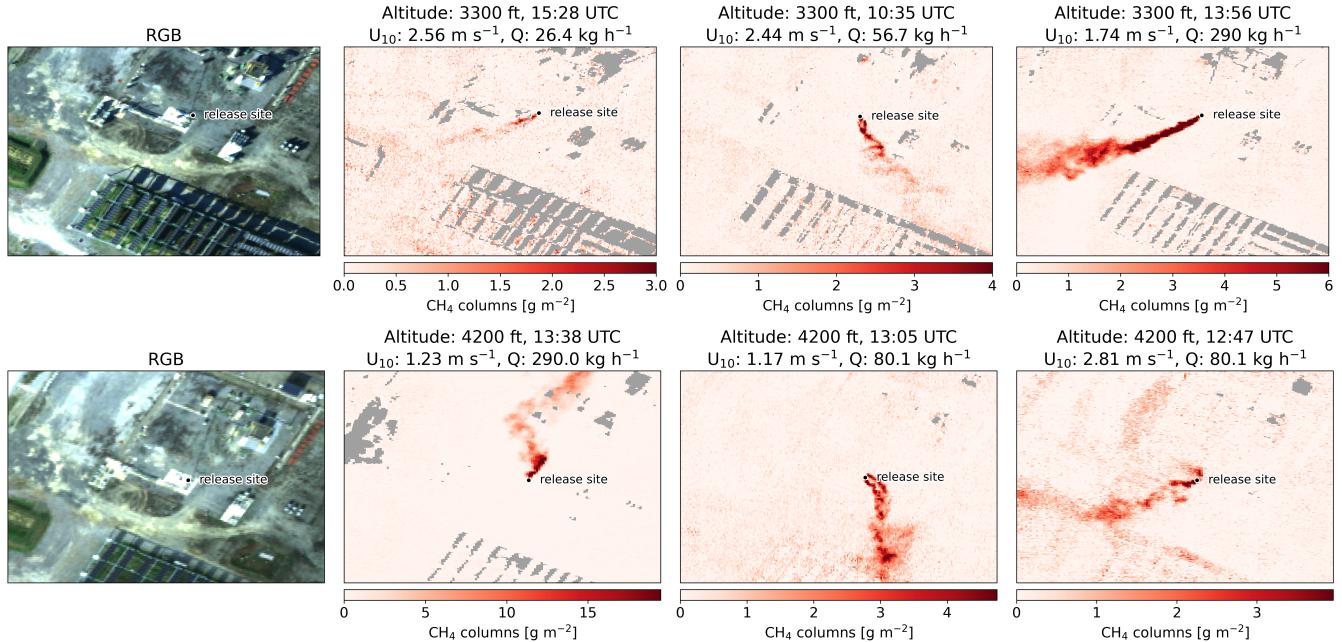
Figure 4. (upper row) Linear CH_4 plumes from release events with 26.4, 56.7 and 290 $kg\,CH_4\,h^{-1}$, observed at 3300 ft at an average spatial resolution of 0.40 to 0.43 m. (lower row) Turbulent CH_4 plumes from release events with 290 and 80.1 $kg\,CH_4\,h^{-1}$, observed at 4200 ft at an average spatial resolution of 0.48 m.

In addition to challenging conditions, there was also a case where turbulence impeded emission estimation, shown in Figure 5. A change in wind direction prior to the overpass appears to have caused a large, dispersed "blob" of CH_4 enhancements. Since these conditions violate the steady-state assumption, this case was excluded from emission estimation.
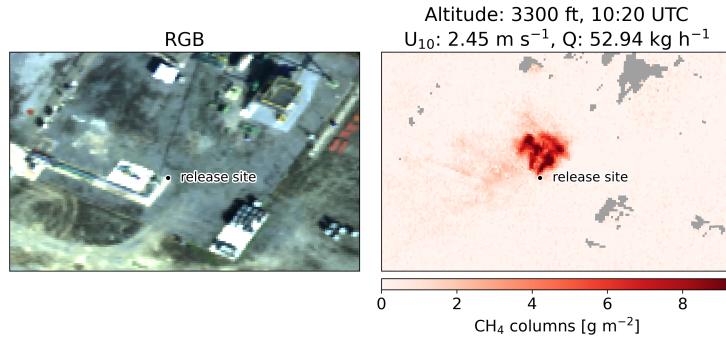
Figure 5. CH_4 plume from release events with $52.94\,\mathrm{kg\,CH_4\,h^{-1}}$, observed at 3300 ft at a spatial resolution of 0.42 m.

3.3 Detection limit

The median noise level of CH_4 maps was estimated to be around ~~700~~450 ppm-m or ~~0.5~~0.3 g $CH_4\,h^{-1}$ for the data of the controlled release experiment. Out of 100 overpasses, plumes were detected on 68 instances (Figure 6). In the most favourable case, the smallest observed plume corresponded to a $1.45\,\mathrm{kg\,CH_4\,h^{-1}}$ release at $U_{10} = 0.76\,\mathrm{m\,s^{-1}}$ and a flight altitude of 4200 ft, representing the best-case detection limit for AVIRIS-4. Under typical conditions, plumes from releases of $5.5\,\mathrm{kg\,CH_4\,h^{-1}}$ and above were consistently detected at altitudes $\leq 4200\,\mathrm{ft}$, with the exception of two overpasses where shadows from surface infrastructure obscured the signal. At higher flight altitudes (6000 - 12000 ft), detection performance was more constrained: for release rates $\leq 9.23\,\mathrm{kg\,CH4\,h^{-1}}$, only one plume was detected (6000 ft, $U_{10} = 1.3\,\mathrm{m\,s^{-1}}$), while the others could not be observed due to the combined effect of higher winds and lower emissions. ~~(a) Reported CH_4 emissions vs. on-site lidar wind measurement at 10 m. (b) Probability of detection for a flight altitude of 1000 m.~~ The original objective of conducting observations at multiple flight altitudes was to determine an altitude-dependent detection limit. However, because the CH_4 release rates were not known in advance, the largest release event captured at all five altitudes was metered at only $9.23\,\mathrm{kg\,CH_4\,h^{-1}}$. This emission rate was below the detection threshold at altitudes above 6000 ft and therefore remained undetectable in those overpasses. ~~As a consequence, no altitude-dependent detection limit could be established.~~ For the overpasses below 6000 ft, we computed the probability of detection (PoD) for AVIRIS-4 according to Conrad et al. (2023) as a function of reported emissions Q_{rep}, U_{10} and flight altitude $\tilde{h}$ using the flags "detected" and "not detected" by optimising the predictor and inverse

link functions. This resulted in the following PoD function which is plotted in Figure 6.

$$315 \quad \text{PoD} = 1 - \left(1 + \left(1.03 \times 10^{10} \right) \frac{\left(5.18 \times 10^{8} \right) Q^{1.93}}{\left(\dfrac{\tilde{h}}{1000} \right)^{3.88} \left(U_{10} + 97.0 \right)^{9.97}} \right)^{-1.84} \quad (21)$$
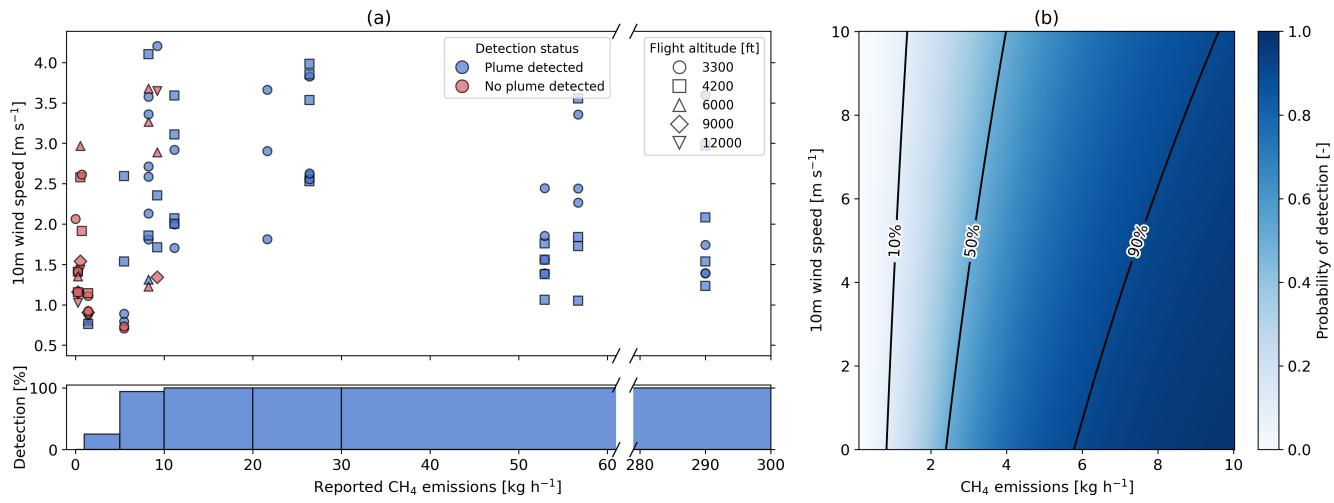
Figure 6. (a) Reported CH_4 emissions vs. on-site lidar wind measurement at 10 m. (b) Probability of detection for a flight altitude of 1000 m. above mean sea level using Eq. 21.

3.4 CH$_4$ emission estimation

We were able to estimate the emission from 67 of the 68 detected plumes, 54 of which were estimated using the CSF method and 13 using the IME method. Figure 7 shows the reported versus estimated CH_4 emissions using four different wind speed
320 inputs. As outlined in Section 2.5, the initial CH_4 emission estimates were calculated using ERA5 U_{10}, shown in subplot (a) of Figure 7. This approach yields a relatively weak correlation, with a fitted slope of only 0.53 and an R^2 value of 0.55. Replacing ERA5 data with lidar-measured U_{10} in subplot (b) of Figure 7 substantially improves the agreement, increasing the slope to 0.65 and an R^2 value of 0.73. This highlights the limitations of reanalysis wind data for accurate emission quantification (further shown in Figure A1). As a result, the use of ERA5 introduces both correlated and uncorrelated uncertainties in emission
325 estimates that are difficult to quantify or correct.

Even when using on-site lidar wind speeds (Figure 7b), biases remain: emission rates for small release events tend to be overestimated, while large releases (e.g. at 80.1 and 290 $\text{kg}\,CH_4\,\text{h}^{-1}$) are significantly underestimated. This behaviour can be explained by plume dynamics: Small release events result in short plumes which remain near the emission height (<10 m for
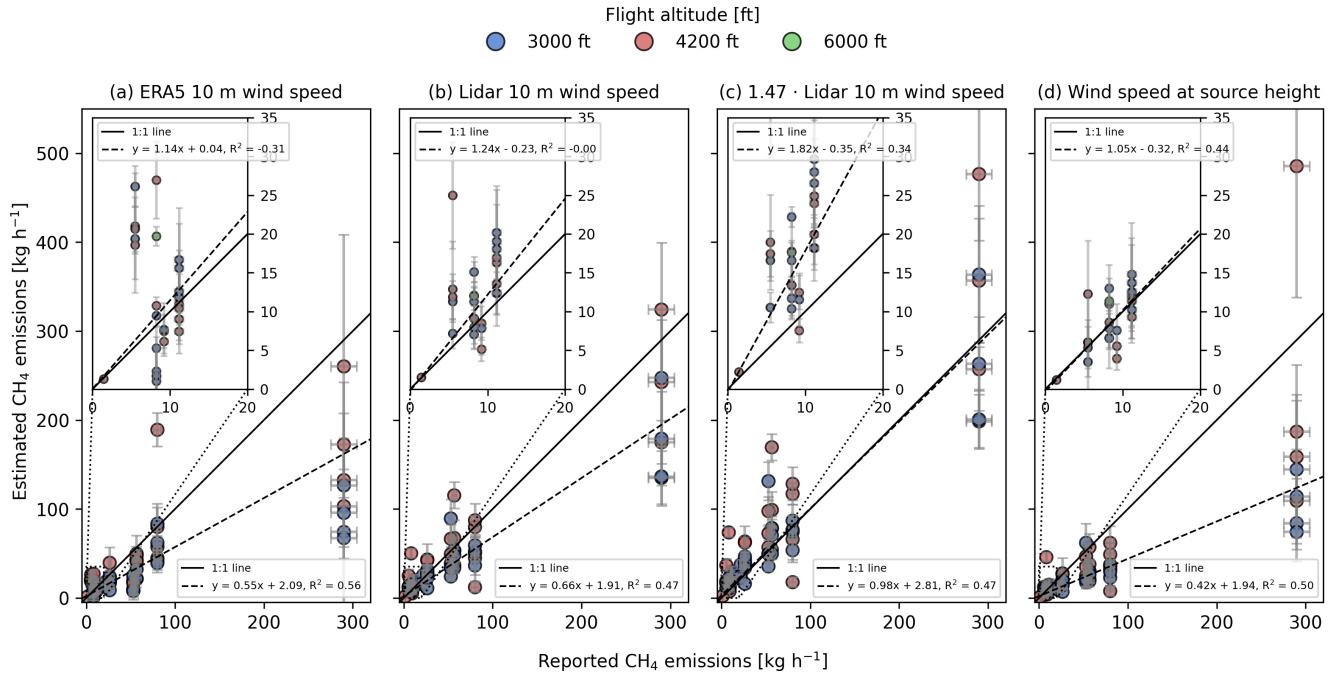
Figure 7. Comparison between reported and estimated CH_4 emissions using (a) ERA5 10 m wind speeds, (b) lidar 10 m wind speeds, (c) effective wind speeds using ~~$1.4 \times u_{10}$~~ $1.47 \times U_{10}$ according to Varon et al. (2018) and (d) effective wind speeds at source height as described in Section 2.5. Insets enlarge the low-emission range and have an independent fit to the emission estimates. It is important to note that the R^2 value represents the coefficient of determination of the weighted regression, which can take negative values.

all releases), making the use of U_{10} prone to overestimation. In contrast, large releases produce longer plumes that undergo
330   greater vertical mixing. The actual effective transport height may thus be above 10 m, resulting in an underestimation of
emissions when using U_{10}. Additional influencing factors are specific to the release equipment, such as the outlet ejection
velocity and whether the emission was oriented horizontally or vertically.

These limitations highlight the importance of estimating an effective wind speed (U_{eff}) that accounts for both source height
and vertical mixing. Subplots (c) and (d) in Figure 7 compare two approaches: the method of Varon et al. (2018), which
335   accounts only for vertical mixing, and the method developed in this study, which accounts only for source height. In subplot
(c), the overall fitted trend lies close to the 1:1 line, but the estimates for small releases are substantially worse than when using
U_{10}. This reflects the fact that Varon et al. (2018) derived the linear relationship between U_{10} and U_{eff} for GHGSat, which has
a coarser spatial resolution (50×50 m). At that scale, plumes have more time to mix vertically and are therefore transported
by winds stronger than U_{10}. In contrast, subplot (d) shows a poorer overall trend than (c) due to the strong influence of large
340   release events, but the estimates for small releases improve considerably. This suggests that short plumes are well captured
because they remain close to the emission height, whereas vertical mixing is insufficiently accounted for in the case of larger
releases.

To further investigate this hypothesis of strong vertical mixing, we incorporated lidar wind speeds at 20 and 38 m and calculated the uncertainty-weighted root mean squared error (RMSE) and relative mean bias error (MBE) between estimated and reported CH_4 emissions, as shown in Figure 8. The results confirm that using U_{src} substantially improves emission estimates for low intensity release events. For release events above $30\,kg\,CH_4\,h^{-1}$, however, using U_{src} tends to underestimate emissions and performs worse than estimates based on U_{10}, U_{20} and U_{38}. Although the relative MBE decreases for larger releases, the high relative RMSE indicates substantial variability around the true values. This pattern may reflect the greater influence of turbulence on longer plumes compared to shorter ones.
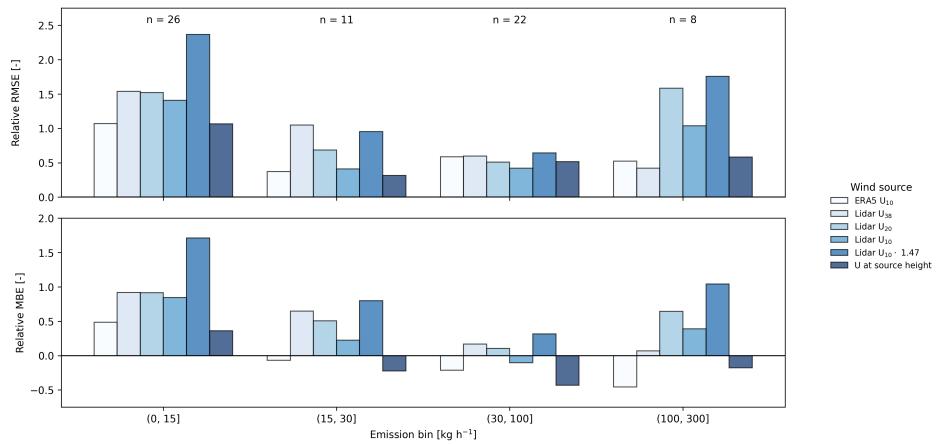
Figure 8. Mean relative root mean squared error (RMSE) and relative mean bias error (MBE) between estimated and reported CH_4 emissions across emission bins.

In addition to source strength and therefore plume length, absolute wind speed appears to significantly influence the accuracy of emission estimates. This is illustrated in Figure 9, which shows the scaling factor required to align estimated emissions with reported values as a function of (a) plume length and (b) effective wind speed. While subplot (a) of Figure 9 supports the previously discussed hypothesis regarding plume length, subplot (b) reveals that lower wind speeds are associated with larger and more variable scaling factors. This observation aligns with the findings of Varon et al. (2018); Sánchez-García et al. (2022); McManemin (2025), who reported reduced accuracy in emission estimates across various techniques under low wind speed conditions. This is likely due to the increased variability typically observed at lower wind speeds. In contrast, we did not observe larger scaling factors for larger coefficients of variation (CoV) in wind direction in subplot (c) of Figure 9 as discussed in McManemin (2025). The reason for this is that our method does not depend on wind direction, as we do a nearly instantaneous measurement. The large spread in angles between the wind direction and the curve fitted to the plume in subplot (d) further highlights the strong influence of wind turbulence on the observed plumes.

This hypothesis is further supported by individual cases where estimated emissions diverge from reported values, as illustrated in Figure 10. Subplot (d) shows that the CH_4 fluxes across different cross-sections fluctuate strongly between 100 and $200\,kg\,CH_4\,h^{-1}$ due to turbulent wind, likely reflecting both temporal variability in wind speed and changes in plume height
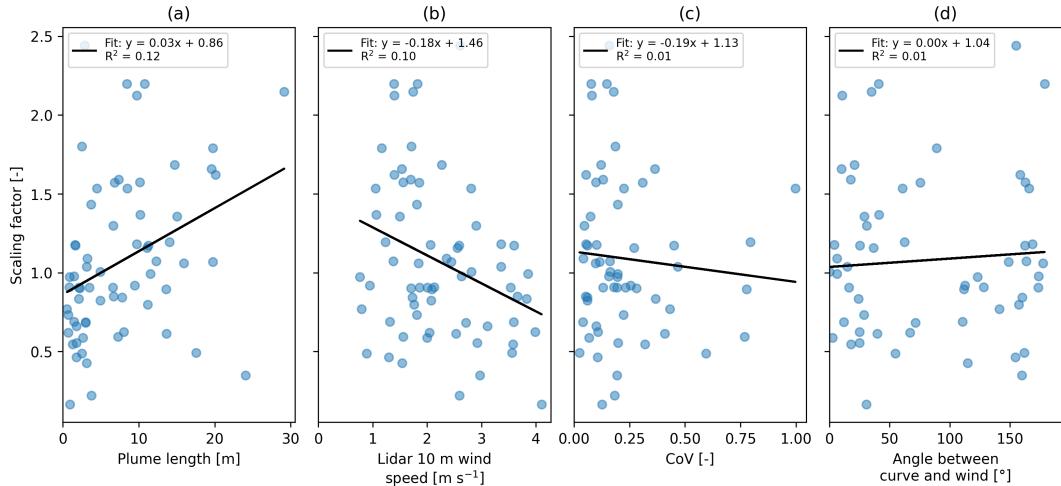
Figure 9. Correlation of (a) plume length, (b) 10 m wind speed, (c) Coefficient of Variation (CoV) and (d) angle between plume curve and wind direction with the scaling factor required to align estimated CH_4 emissions using ~~Lidar~~ lidar 10 m wind speeds with reported values.

that exposed it to different wind regimes. In such cases, one might consider using only CH_4 enhancements close to the source, such as those from the first cross-section, where U_{eff} is expected to better approximate the wind speed at source height. However, this example shows that even this approach leads to underestimation, indicating that the measured wind speeds do not accurately reflect actual wind conditions. An analysis of the wind speed during the two minutes of the overpass reveals that U_{10} varies between 1 and 3 ~~$m\,s^{-1}$~~ m s^{-1}. For comparison, a 20 m plume under a 1 m s^{-1} wind has a residence time of about 20 s, which matches the sampling interval of the wind lidar. As a result, the wind speed fluctuations visible in the plume cannot be resolved by the lidar, and the underestimation can likely be attributed to larger-than-expected temporal variability that is not captured at the instrument's temporal resolution.

The analysis of uncertainty contributions to total emission estimate uncertainty (Figure A2) indicates that wind speed is the dominant factor for both the CSF and IME methods. Most of this contribution arises from the natural variability of wind speed, with additional influence from uncertainty in the effective wind speed. In comparison, measurement errors in wind speed account for only a minor portion of the overall uncertainty.

Lastly, one source of deviation between estimated and reported CH_4 emissions is the presence of cloud shadows over the release site as shown in Section 3.5.3, leading to the strong underestimations of the 80.1 kg CH_4 h^{-1} release event observed in Figure 7. Despite this underestimation, the plumes were still reliably detected, indicating that observations under suboptimal cloud conditions can still be valuable e.g. for leak detection.
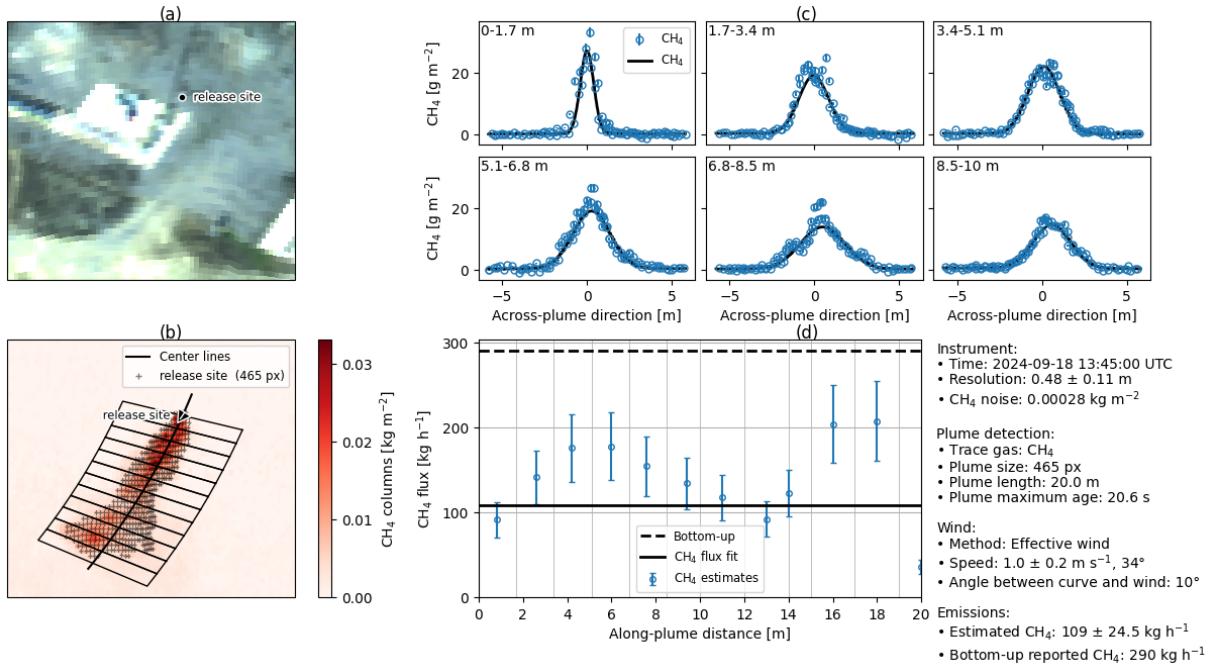
Figure 10. (a) RGB image of the release location, (b) CH$_4$ map showing the detected plume and 12 cross-sections, (c) Gaussian fits to the CH$_4$ columns from the first and last three cross-sections, (d) along-plume flux of all cross-sections and retrieval metadata.

3.5 Factors affecting the CH$_4$ retrievals

3.5.1 Spatial resolution

Figure 11 shows examples of AVIRIS-4 RGB images and CH$_4$ maps of the release site acquired at 12000, 9000, 6000, 4200, and 3300 ft in the afternoon of the 16th of September. The across-track resolutions are 2.0, 1.5, 1.0, 0.7, and 0.5 m, while the along-track resolution is approximately 0.4 m. For the overpasses at 12000 and 6000 ft, the across-track resolution is represented on the x-axis, whereas for the others it is represented on the y-axis. Black circles indicate an ~~artifact~~ artefact caused by a white object located at the release site. This ~~artifact~~ artefact arises because, first, the reflectance signal appears to correlate with the CH$_4$ signal, and second, the high albedo of the object leads to increased radiance, which in turn produces an artificially elevated enhancement in the CH$_4$ maps. At higher altitudes (12000 and 9000 ft), the spatial resolution is too coarse to clearly distinguish this artefact from a true enhancement. The CH$_4$ plume from the release event with an emission rate of $9.23\,\mathrm{kg\,CH_4\,h^{-1}}$ is only visible at higher spatial resolutions during overpasses at 3300 and 4200 ft.
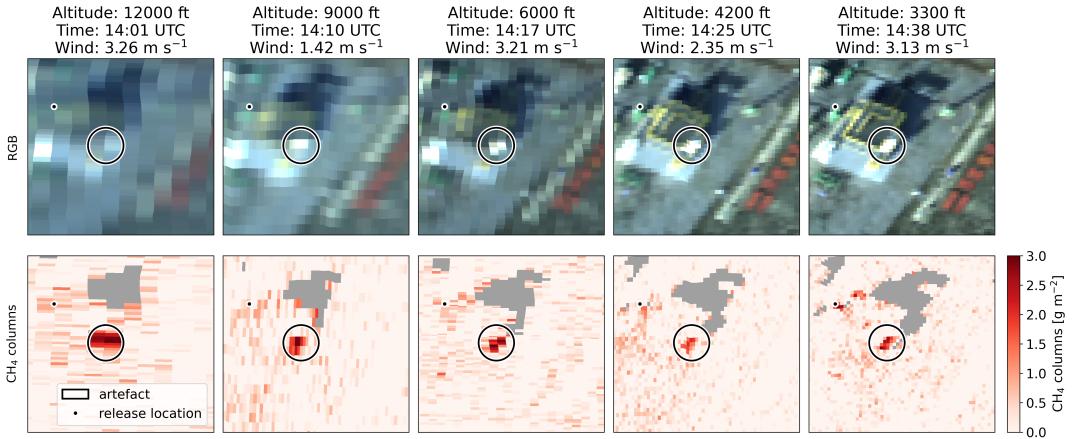
Figure 11. RGB images and CH_4 maps for different flight altitudes with average spatial resolutions of 2.0, 1.5, 1.0, 0.7 and 0.5 m across-track and 0.35 m along-track. All observations are from a release event on the 16th of September with reported emissions of $9.23\,\mathrm{kg\,CH_4\,h^{-1}}$

3.5.2 Cast shadows

The cast shadows of buildings and objects are clearly visible at high spatial resolution. Shadows compromise the CH_4 retrieval, which assumes a non-scattering atmosphere, since light in shadowed areas originates solely from scattering. Therefore, an efficient shadow masking is necessary at these resolutions. Figure 12 shows the effect of the shadow mask for a scene with water bodies and cast shadows and the release site with a nearby photovoltaic plant. It can be seen that the masking of cast shadows and dark surfaces such as solar panels is important to prevent biases in the CH_4 maps which would interfere with plume detection. Furthermore, in instances where the plume coincides with shadowed areas, the artificially elevated enhancements would skew emission estimates. As a result of the shadow mask, CH_4 emissions can also be estimated if the plume is transported over shadowed areas.

The downside of shadow masking is that some short plumes of small release events could not be detected because they aligned with shadows. Furthermore, depending on the threshold used for shadow masking, surfaces with low albedos could be masked, preventing the detection of CH_4 emissions.

3.5.3 Cloud shadows

During all eight overpasses of the $80.1\,\mathrm{kg\,CH_4\,h^{-1}}$ release on the 19th of September, cloud shadows intersected the flight line while on five out of eight overpasses, cumulus clouds obscured the sun over the release site. Under such conditions, the measured radiance is dominated by scattered light, violating the assumptions used in calculating the target spectrum. Moreover, cloud shadows on the flight line render the mean spectrum $\hat{\mu}$ unrepresentative of the observed radiance L_{obs} over the release site. Consequently, subtracting $\hat{\mu}$ from L_{obs} in Eq. 2 partially removes the CH_4 signal. This effect is evident in Figure 13, which contrasts an overpass with obscured sun at 13:00 UTC with a clear-sun overpass at 12:54 UTC. The lower row shows
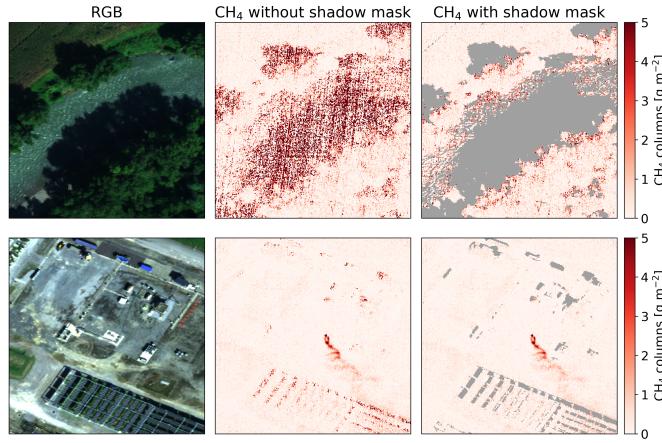
Figure 12. Examples of scenes containing cast shadows and water bodies (upper row) and the release site during a release event with $56.7 \, \mathrm{kg \, CH_4 \, h^{-1}}$ (lower row), without and with shadow masking.

$L_{\mathrm{obs}} - \hat{\mu}$ over the same plume-free area in both cases. As can be seen, the cloud shadow strongly reduces the signal. As a result, emission estimates for shadowed cases, or for scenes with a substantial fraction of cloud shadows along the flight line, tend to be underestimated. Consequently, a refined retrieval algorithm would be necessary to provide unbiased CH_4 maps and emission estimates.
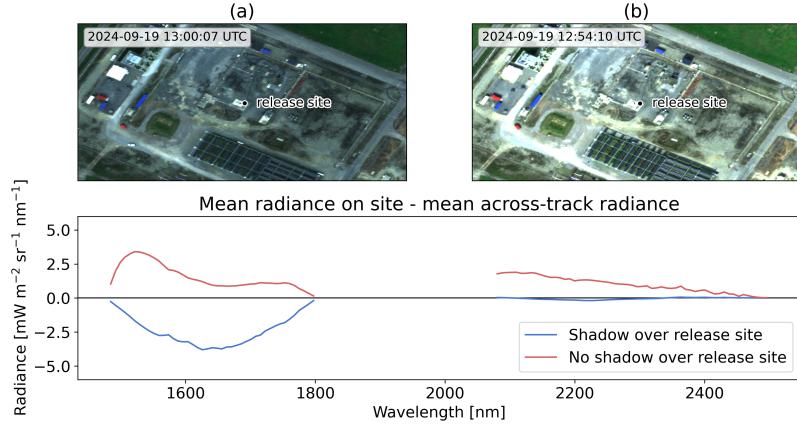
Figure 13. RGB image of $80.1 \, \mathrm{kg \, CH_4 \, h^{-1}}$ release on the 19th of September (a) with and (b) without cloud shadow. The lower row shows the mean $L_{\mathrm{obs}} - \hat{\mu}$ over the same plume-free area within the wavelength window used for CH_4 retrieval for both cases.

3.5.4 Plume shadows

415 As a consequence of the unprecedentedly high spatial resolution of AVIRIS-4 and the high SZA for some of the overpasses (see Figure 2), we discovered that, out of 68 detected plumes, 13 were found to contain two plumes that were occasionally overlapping and occasionally distinct, as illustrated in Figure 14. This phenomenon can be explained as plume shadows: One
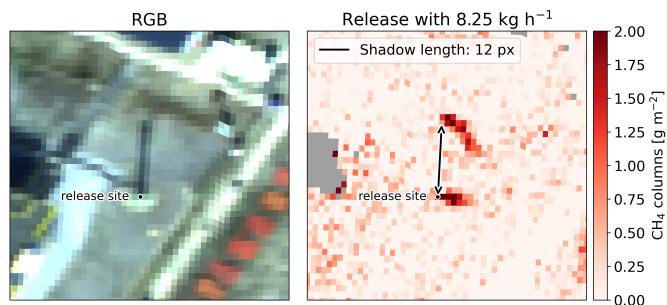
Figure 14. Left: RGB image of the study site with a marker on the release location at 6.5 m above ground. Right: CH_4 map of the study site with two plumes visible.

plume appears at the actual release location and corresponds to the CH_4 absorption signal of the light path that first travels from the sun to the ground and, after being reflected, passes through the plume. The second plume is observable at the upper end of

420 the shadow cast by the pole of the source. This plume corresponds to the absorption signal of the light that first passes through the plume, is then reflected from the ground and reaches the sensor without passing through the plume a second time. This phenomenon has been shown in simulations by Schwaerzel et al. (2020) and first observed by Sánchez-García et al. (2022). It is important to note that the effect of light passing through the plume only once instead of twice occurs under all conditions with sufficiently high SZA. For sensors with coarse spatial resolution, however, the plume and its shadow cannot be resolved

425 separately and have therefore never been explicitly considered in CH_4 retrieval or emission estimation prior to this study. To correct for plume shadows, we applied the method outlined in Section 2.4.4 to the four observed plumes that were clearly separated. This resulted in a mean correction factor of 2.6.

3.5.5 MF vs. LMF

For the analysis of this study we also tested the LMF which was developed by Schaum (2021) and tested in Pei et al. (2023). The

430 plume images using the MF and LMF in Figure 15 show that smaller enhancements (upper row) can be detected more reliably and accurately using the LMF as worked out in Schaum (2021). In our case, the LMF enabled the detection of a release as small as 1.45 kg CH_4 h^{-1} at a flight altitude of 4200 ft. This improved detectability can be attributed, in part, to reduced ~~noise levels in the~~ random background variability in the retrieved CH_4 ~~retrievals~~maps, which facilitated more confident identification of the plume signal. However, the LMF also ~~increases~~ introduces larger systematic biases in background CH_4 values compared to the

435 MF, as evident in both the upper and lower rows of Figure ~~15.~~ 15. An analysis of the eigenvalues of the covariance matrices for

different surface albedos suggests that these biases are associated with increased sensitivity of the log-transformed radiances to pixels with low SNR, which is the case for albedo surfaces with low albedo. Additionally, we observed that the LMF had little to no effect on CH_4 enhancements for the largest release events in the campaign, such as the 290 kg CH_4 h^{-1} release. This is likely because ~~these stronger enhancements remained within the linear absorption regime of CH_4, where the standard MF already performs effectively~~ our iterative MF already compensates for most of the non-linear absorption associated with high optical depths.
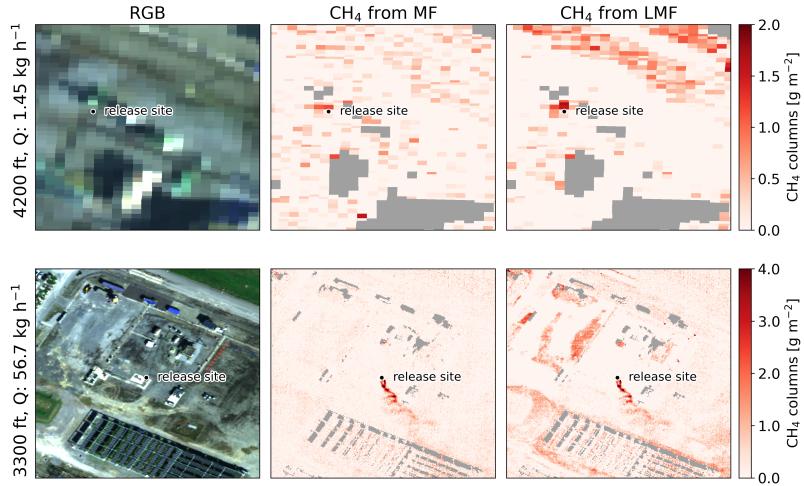
Figure 15. RGB images and CH_4 maps obtained from MF and LMF for release events with 1.45 and 56.7 kg CH_4 h^{-1}, observed at 4200 and 3300 ft. Note that the upper row shows a zoomed-in subsection of the scene to be able to see the short plume.

3.6 Estimating the source height from (plume) shadows

The high spatial resolution of AVIRIS-4 offers the unique opportunity to estimate the height h of an emission source based on the length of the shadow l_s in the RGB image (Figure 14a) cast by the emission source using trigonometry:

$$h = \frac{l_s}{tan(\text{SZA})} \tag{22}$$

Alternatively, the height can be estimated in the same way from the horizontal separation of the starting points of the two plumes (Figure 14b). With increasing distance, the two plumes move together more closely, suggesting that the plume is pushed towards the surface directly after the release. Knowledge of the emission height is an important parameter for emission estimation, as it can be used to determine the effective wind speed, which is a critical input for estimation estimation. In the example shown in Figure 14 with an SZA of 50° and a spatial resolution of 0.53 m, the emission plume at the stack must be 6.4 ± 1.1 m above ground which is in agreement with the true emission height of 6.5 m.

We assume that this technique can be ~~applied if the length of the shadow is at least twice as large as the uncertainty in the length of the shadow σ_{l_s}~~ reliably applied only if the measured shadow length exceeds its measurement uncertainty by a

~~sufficient margin~~. The uncertainty in ~~turn is given as the number of pixels with resolution l_p which contain both shadow and illuminated surface, which is~~ the shadow length is dominated by pixel discretization at the shadow boundaries, where at most one ~~at the top and one at the bottom~~ mixed pixel can occur at both the upper and lower edge of the shadow. ~~Therefore~~Requiring the shadow length to be at least twice this uncertainty ensures that the shadow is sufficiently resolved. Under this criterion, the minimum emission height ~~becomes~~ that can be resolved is given by

$$h > \frac{2 \cdot l_p}{tan(\text{SZA})} \tag{23}$$

For the campaign discussed in this study, this minimum height is shown in Figure 16.
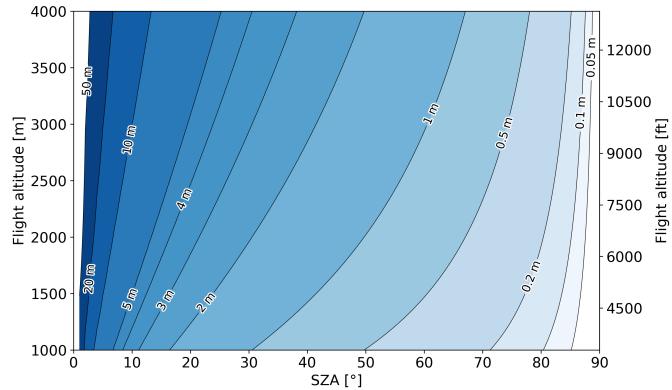
Figure 16. Minimum source height in metres above ground at which shadows of emission sources extend over more than one pixel, shown as a function of SZA and flight altitude above mean sea level.

4 Discussion

4.1 Capabilities and limitations of AVIRIS-4

Following the success of the AVIRIS Classic and AVIRIS-NG sensors in detecting and quantifying CH_4 emissions as demonstrated in numerous previous studies, this study explores the potential of their successor, AVIRIS-4. Although AVIRIS-4 was primarily developed for surface and vegetation studies, our results show that CH_4 columns can be determined with an unprecedentedly high spatial resolution, enabling the detection of short plumes from low intensity sources. In combination with the enhanced SNR, the detection limit is reduced to 5.5 $\text{kg}\,CH_4\,\text{h}^{-1}$ under good weather conditions and down to below 1.5 $\text{kg}\,CH_4\,\text{h}^{-1}$ under ideal conditions. Because the campaign took place in mid-September, we expect the detection limit could be further reduced under more favourable illumination conditions. As discussed in Section 3.3, we were not able to determine an altitude-dependent detection limit for AVIRIS-4, which complicates direct comparisons with other airborne sensors. For instance, studies with AVIRIS-NG operated at altitudes between 3000 and 6000 m report detection limits of 10-16 $\text{kg}\,CH_4\,\text{h}^{-1}$ under favourable wind conditions (e.g. Ayasse et al., 2023; Conrad et al., 2023). In our case, the lowest release

of 9.23 kg CH$_4$ h^{-1} could not be detected at a comparable altitude of 2740 m, likely due to higher wind speeds. This makes it difficult to assess whether and by how much the detection limit has improved. In Thorpe et al. (2016), the lowest detected release was 2.3 kg CH$_4$ h^{-1}, but at a much lower flight altitude of 430 m and under higher wind speeds of 3-5 m s^{-1}. Kuhlmann et al. (2025) report a detection limit of 15 kg CH$_4$ h^{-1} at a flight altitude of 6000 m with wind speeds of 0.5 m s^{-1}. Overall, comparing detection limits across studies is challenging, as they depend strongly on flight altitude, wind speed, and spectral albedo (Conrad et al., 2023).

Decreasing the detection limit is pivotal because low intensity CH$_4$ sources are more numerous than high-emitting ones (e.g., Williams et al., 2025; Kuhlmann et al., 2025). Consequently, accurate estimates of total CH$_4$ emissions depend on detecting smaller sources. For instance, based on the best detection limit of AVIRIS-NG of 15 kg CH$_4$ h^{-1} reported in Kuhlmann et al. (2025) and the distribution of oil production sites in Romania across the outlined scenarios, AVIRIS-NG was able to detect between 45% and 62% of total emissions. In contrast, assuming a detection limit of 5.5 kg CH$_4$ h^{-1}, AVIRIS-4 would increase this detection coverage to approximately 67%–81%. Moreover, the detection limit of 5.5 kg CH$_4$ h^{-1} achieved by AVIRIS-4 effectively enables the identification of all point sources listed in the E-PRTR registry, which mandates reporting for emissions exceeding 100000 kg CH$_4$ yr^{-1} (equivalent to 11.4 kg CH$_4$ h^{-1}) (European Parliament and the Council of the European Union).

~~In comparison with its predecessor, AVIRIS-4 has compromised some of its spectral resolution in order to enhance its spatial resolution and SNR.~~ This study, along with comparisons to other airborne imaging spectrometers with higher spectral but lower spatial resolution such as MAMAP2DL (e.g. Krautwurst et al., 2024), demonstrates that ~~this~~ the trade-off of higher spatial and slightly lower spectral resolution is beneficial for detecting small-scale CH$_4$ enhancements from low intensity sources, whose plumes typically extend only a few decimetres to a few metres.

The noise level of the CH$_4$ maps was estimated as the standard deviation of the retrieved columns over the brightest 50% of pixels. This resulted in a noise level of AVIRIS-4 of ~~700~~450 ppm-m at an average resolution of 0.5 m which is comparable to reported values of AVIRIS-NG at 5 m resolution for suboptimal illumination conditions (e.g. Borchardt et al., 2021). Such noise levels are expected, given that the campaign was conducted in mid-September under low solar zenith angles (SZAs). In addition, negative values were not masked during the CH$_4$ retrieval, which increases the apparent noise.

The current study also shows that owing to the higher SNR and higher spatial resolution, emissions can also be detected and estimated with less illumination and under suboptimal surface and atmospheric conditions, which are characterised by inhomogeneous albedo, strong turbulence, cast shadows and cloud shadows (see Section 3.1), compared to previous controlled release experiments with AVIRIS-NG (e.g. Thorpe et al., 2016; Duren et al., 2019). For example, the higher spatial resolution allows for a more accurate filtering for shadow pixels and albedo artefacts which, if undetected, could lead to biases in emission estimates, as outlined in Section 3.5.2. This capability allows AVIRIS-4 to be effectively applied to built-up sites with heterogeneous surface albedo and cast shadows, conditions commonly encountered around CH$_4$ sources in the oil, gas, and coal mining sectors.

However, the higher spatial resolution also results in new challenges. One of them is the ~~double plume~~ occurrence of double plumes originating from plume shadows illustrated in Figure 14. We corrected for this ~~artifact~~ artefact when the true plume

and its shadow were clearly separated, but its impact on retrieved CH$_4$ enhancements requires further analysis. ~~Additional~~ In this context, a recent study by Gorroño et al. (2025) systematically investigated the effect of different observation and illumination geometries on the retrieved CH$_4$ maps (i.e. parallax effect) and the resulting emission estimates. They showed that large VZAs and SZAs can lead to artificial elongation or compression of plumes along the plume direction. This bias in apparent plume length L directly propagates into emission estimates and likely also occurred in the observations analysed in this study. However, their influence is probably masked by the comparatively large variability in wind speed. Furthermore, Gorroño et al. (2025) found that the parallax effect substantially reduces the PoD due to lower apparent CH$_4$ enhancements. In their simulations, the PoD varied between approximately 0.5 and 0.8 depending on the angular configuration. For the present study, the influence of parallax effects is likely minor, as the detection outcomes shown in Figure 6 are primarily controlled by wind speed and flight altitude. The few non-detected plumes with emission rates exceeding $5\,\mathrm{kg\,CH_4\,h^{-1}}$ at low wind speeds are instead attributable to overlaps with retrieval artefacts. Gorroño et al. (2025) also demonstrated that when the effective wind speed U_{eff} is calibrated against the $10\,\mathrm{m}$ wind speed U_{10} using L, biases in L translate into systematic errors in the calibration itself. As a consequence, emission estimates exhibit errors below 10% for mid-latitude summer conditions, but can reach up to 30% for wintertime observations. In the context of this study, the parallax-induced bias in U_{eff} is only relevant for emission estimates derived using the U_{eff} parametrisation of Varon et al. (2018) and does not affect estimates based on wind speeds at the source height. To mitigate the effect of viewing geometry, Gorroño et al. (2025) recommended to explicitly account for observation and illumination geometry in the planning of flight paths for airborne sensors and to calibrate U_{eff} using plume simulations that match the angular configuration ("train as you measure"). Overall, additional work is needed to ~~handle partially overlapping plumes~~correct for the parallax effect, especially as ~~the phenomenon of plume shadows~~ this phenomenon also affects instruments with coarser spatial resolution even if they do not spatially resolve the plume shadow (Schwaerzel et al., 2020).

A second challenge that arises with higher spatial resolution are the higher per-pixel enhancements for larger sources. As a result, the linearisation of the unit absorption spectrum around $\alpha = 0$ no longer holds and assumed enhancements for the calculation of the absorption spectrum have greater influences on the retrieved enhancements. Therefore, careful selection of the assumed enhancements, e.g. with the iterative approach used in this study, is essential.

Lastly, the current study shows mixed results when using the LMF introduced by Schaum (2021). On the one hand, the proposed improvement for the detection of weak plumes was also observed in this study and lowered the detection limit even under challenging conditions. On the other hand, the LMF increased local biases in the retrieved CH$_4$ maps which ~~would impede the (automated) detection of plumes as it introduces elevated background levels that can obscure smaller enhancements or cause false positives in regions with complex spatial patterns. Additionally, the~~ we attribute to the amplification of noise by the log-transform in pixels with low SNR, caused by low albedo. This spatially more heterogeneous background can obscure small enhancements or produce false detections. In contrast to Schaum (2021), we did not observe an improved performance of the LMF for ~~larger sources reported by Schaum (2021) was not observed. Further~~ large release events. The iterative MF applied in our study seems to successfully account for most non-linear absorption in pixels with large CH$_4$ enhancement. Therefore, further systematic analyses will be required to ~~determine under which circumstances the LMFmethod can outperform the more~~

~~established MF~~ develop approaches that reduce or correct for this noise amplification in the LMF. Other approaches, such as WFM-DOAS (e.g. Borchardt et al., 2021), may also help better account for non-linear effects arising from strong emission sources. However, they are computationally more expensive than the MF and tend to work better for sensors with higher spectral resolution.

4.2 Wind speed estimation

As seen in Section 3.4, estimated emissions linearly depend on the wind speeds used. Therefore, accurate estimates of wind speeds are crucial for accurate emission estimates. Additionally, our analysis demonstrated that uncertainties in wind speeds contributed disproportionately to the uncertainty of the estimated emissions. Based on the analysis of this study, the wind speed representation error (σ_{repr}), uncertainties in effective wind speed (σ_{eff}) and instrument precision (σ_{inst}) likely need to be revised upward. Consequently, building on the understanding of wind speed inputs (see Section 4.2.1), future research on emission estimation from remote sensing data should prioritise methods for deriving the effective wind speed that governs plume transport (see Section 4.2.2).

4.2.1 Source of wind speed estimates

As clearly illustrated in Figure A1, near-surface winds can be be highly variable and gusty. We frequently found that U_{10} measured by the ~~Lidar~~ lidar varied between 1.0 and 3.0 ~~$m\,s^{-1}$~~ ms^{-1} within one minute. These rapid fluctuations highlight that reanalysis wind fields are insufficient for high-resolution emission estimates with new-generation sensors, as they can introduce substantial biases. A high-resolution model may be able to represent this gustiness more realistically in a statistical sense, but capturing the actual wind conditions at the moment of the overpass remains practically impossible. Alternatively, wind speed data from existing measurement networks could be used for emission estimation. However, these networks have varying data quality and might not be available in the vicinity of a CH_4 source. Therefore, one could employ mobile instruments as it was used for the controlled release experiment in the current study. Even if this would provide the most accurate estimate of the wind speed, setting up wind speed instrument would negate the advantage of remote sensing instruments which is to image extensive areas and estimate the emissions of a large number of sources. Additionally, the current analysis has shown that under turbulent conditions, wind speed representation errors can be substantial, even when wind measurements are taken just 100 m from the source. Therefore, the best approach would be to measure wind speed profiles in tandem with imaging spectrometry, e.g. by using an airborne wind lidar as investigated in Thorpe et al. (2021).

4.2.2 Effective wind speeds

In addition to determining the small-scale and short-term wind speeds, a further challenge is to determine the effective wind speed at which the plume was transported. Although an increasing number of studies attempt to derive ~~U_{eff}~~ U_{eff} from model simulations (e.g. Varon et al., 2018; Guanter et al., 2021; Sánchez-García et al., 2022; Ayasse et al., 2023; Guanter et al., 2025), none has systematically investigated the effect of emission height, atmospheric stability or surface roughness on U_{eff}.

Moreover, existing simulations lack the spatial and temporal resolution required for AVIRIS-4 applications. To advance our understanding of the effective wind speed, high-resolution model studies are needed to analyse the impact of the aforementioned factors. Ideally, these results could be parametrised to estimate the effective wind speed based on known driving factors. While estimates for the 3D wind field, surface roughness and heat fluxes could be obtained from regional weather prediction models, information about the emission height could be obtained directly from AVIRIS-4 imagery as outlined in Section 3.6. Another innovative approach has recently been demonstrated in Eastwood et al. (2025) with AVIRIS-3 where a single plume was observed multiple times during one overpass by adjusting the flight path of the aircraft. Specifically, the aircraft ascended while approaching the plume, maintained a level trajectory while flying directly over it, and then descended after passing it. From the resulting three images, the plume velocity was estimated by calculating optical flow vectors for consecutive CH_4 images. While this method proved to significantly improve the estimates of the effective wind speed compared to reanalysis data and on-site wind lidar data, it requires a-priori knowledge of the source location to plan the required flight manoeuvres. One workaround would be to use real-time in-flight retrieval of CH_4 (e.g. Thompson et al., 2015) in combination with pitching AVIRIS-4 using the already installed stabilisation platform. Alternatively, machine learning based models could be used to estimate trace gas emissions either directly from radiance data (e.g. Joyce et al., 2023; Rouet-Leduc and Hulbert, 2024) or from plume images (e.g. Jongaramrungruang et al., 2022; Bruno et al., 2024; Ouerghi et al., 2025; Plewa et al., 2025). These approaches have recently shown that it is possible to infer emission rates without explicitly relying on external wind data. Their main advantages are that they can, just as the other approach outlined above, bypass wind speed uncertainties and additionally, provide rapid and automated emission estimates at large scales. While these models are very promising, they are still limited in their representativeness due to a lack of wind speed information within a single image. Furthermore, they provide limited interpretability and their uncertainty quantification is still less mature than for the traditional approaches based on the mass balance.

5 Conclusions

Detecting and quantifying the emissions from a large number of sources is essential for obtaining accurate inventories of CH_4 emissions. The current study shows that AVIRIS-4 can be used for the improved detection of CH_4 emissions and subsequent quantification. The combination of high spatial resolution with the unprecedentedly high SNR of AVIRIS-4 decreases the detection limit of AVIRIS-4 to below 5.5 $\mathrm{kg\,CH_4\,h^{-1}}$ under good weather conditions and down to 1.5 $\mathrm{kg\,CH_4\,h^{-1}}$ under ideal conditions. This is below the 10 - 16 $\mathrm{kg\,CH_4\,h^{-1}}$ detection limits reported for its predecessor AVIRIS-NG in previous studies. In practice, AVIRIS-4 therefore extends the range of reliably detectable point sources by approximately a factor of two to three relative to AVIRIS-NG when flown at low altitudes, which effectively enables the identification of all point sources listed in the E-PRTR registry. As a result, previously undetected low intensity and dispersed sources can be identified and accounted for in emission budgets. We demonstrate that the high spatial resolution of AVIRIS-4 enables its effective use under challenging conditions and in heterogeneous environments, which are frequently encountered in real-world applications. Furthermore, we show how high-resolution AVIRIS-4 data can be used for the estimation of the source height which is critical information when

estimating the effective wind speed. As with earlier sensors and algorithms, emission estimation with AVIRIS-4 is affected by uncertainties in the estimation of the effective wind speed, especially at the short length and timescales presented in this study. Overall, this study highlights that AVIRIS-4 represents a significant step forward in airborne methane remote sensing, offering unprecedented sensitivity to low-intensity sources under challenging conditions. At the same time, it underscores the importance of advancing wind speed estimation techniques and improving retrieval strategies to fully exploit the sensor's capabilities. Future work should therefore focus on integrating AVIRIS-4 observations with dedicated wind measurements and adapting the CH_4 retrieval algorithm to the unprecedentedly high spatial resolution.

Code availability. The *ddeq* version 1.0 used for this study is available on Gitlab.com (https://gitlab.com/empa503/remote-sensing/ddeq). The code for AVIRIS-4 data processing and CH_4 retrieval is available on request.

Data availability. ERA5 data are available at https://doi.org/10.24381/cds.adbb2d47 (Hersbach et al., 2018). The retrieved AVIRIS-4 CH_4 maps, wind and sources data and estimated emissions are available on the Zenodo data repository (DOI: 10.5281/zenodo.16410532).

Appendix A: Additional figures

Figure A1 reveals substantial systematic deviations, particularly during daytime, likely caused by small- to mesoscale atmo-
spheric circulations influenced by local terrain. Such features are not captured by the relatively coarse spatial ($0.25° \times 0.25°$)
and temporal resolution of ERA5. Furthermore, ERA5 fails to resolve turbulent fluctuations in near-surface winds that are
evident in lidar observations.
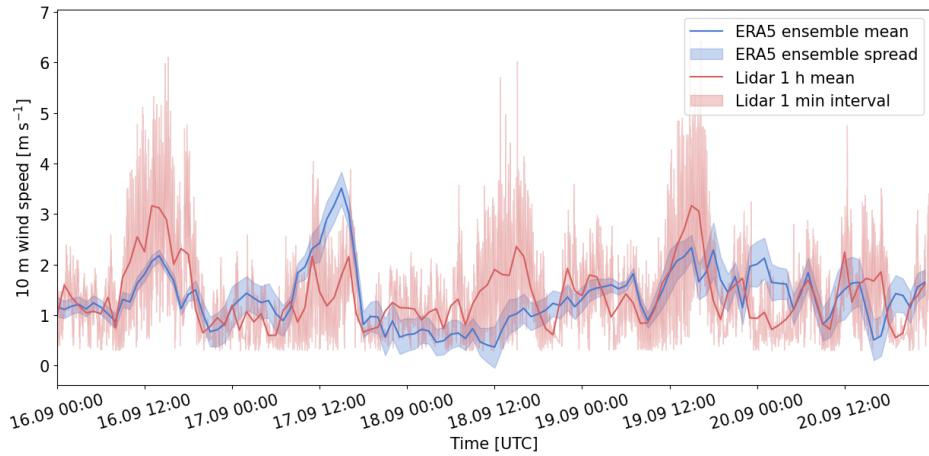
Figure A1. ERA5 U_{10} vs. on-site lidar U_{10}. The blue shaded area represents the ERA5 ensemble spread while the red shaded area depicts
the min and max wind speed for 1 minute intervals.

Figure A2 shows that the uncertainty in the wind speed σ_U contributes 99.4% to the total uncertainty of the estimated
emissions σ_q for the CSF and 91.3% for the IME. σ_U in turn consists 90.4% of natural wind speed variability σ_{var}.
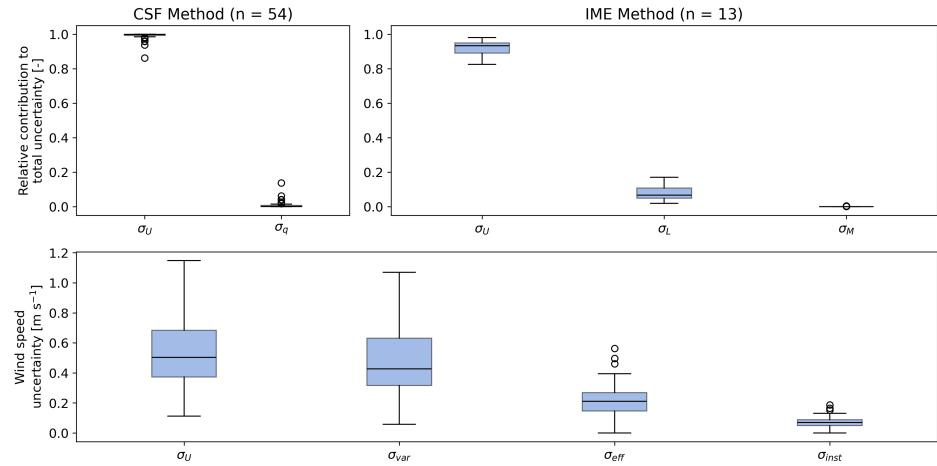
Figure A2. Top row: Relative contribution of the individual uncertainty terms of the CSF and IME to the uncertainty of the estimated emissions Q. Bottom row: wind speed uncertainty contributions by natural variability σ_{var}, effective wind speed σ_{eff} and instrument precision σ_{inst}
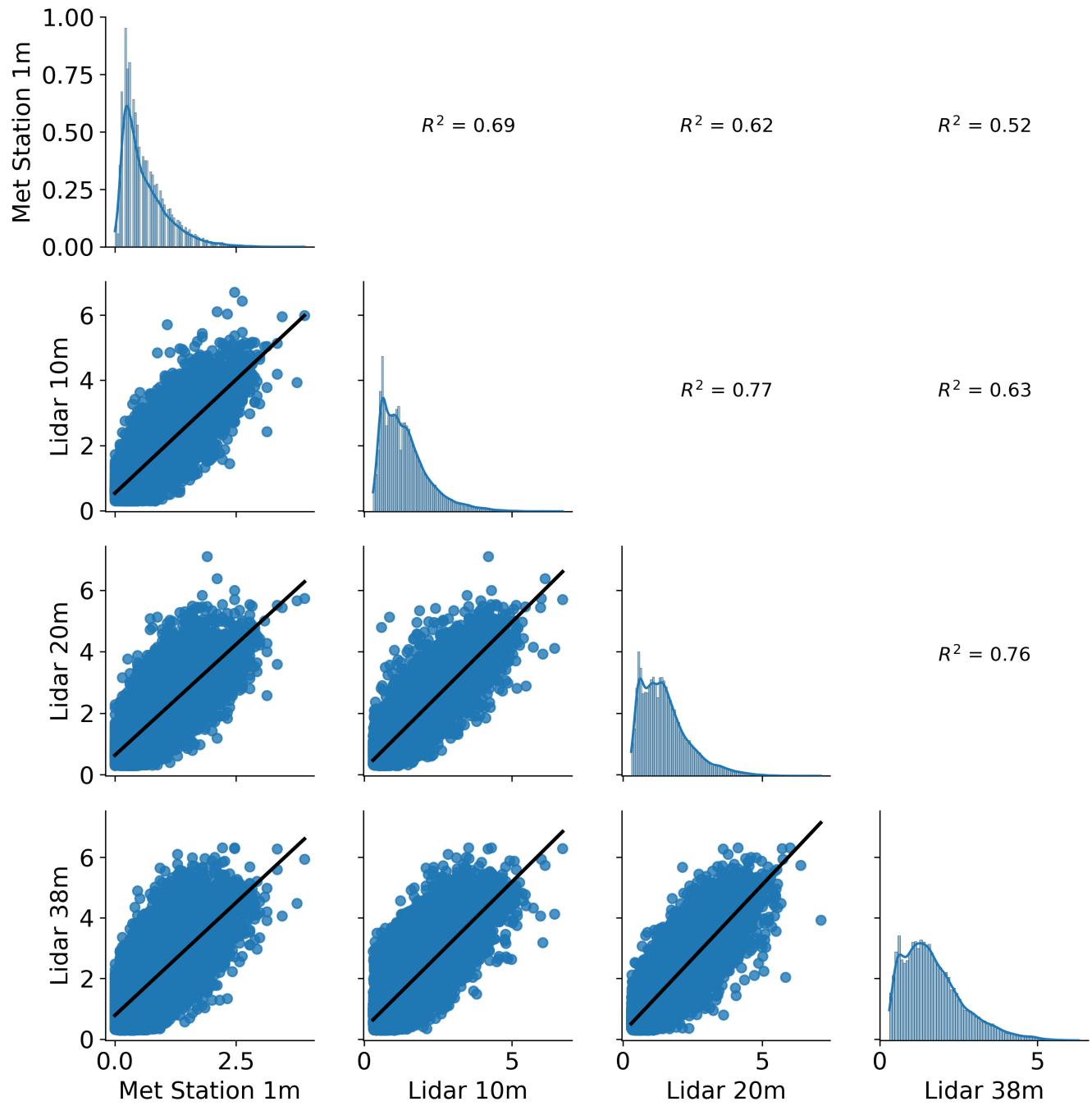
Figure A3. Pair plot of the wind speeds measured by the wind lidar at 10 and 20 m as well as from a meteorological station affixed to the lidar, approximately 1 m off the ground.

Lidar 10 m wind speed [m s^{-1}]					
	16.09.2024	17.09.2024	18.09.2024	19.09.2024	20.09.2024
09:00	N/A	1.1 ± 0.5	1.7 ± 0.6	1.5 ± 0.3	1.8 ± 0.4
10:00	N/A	1.4 ± 0.4	0.9 ± 0.3	0.9 ± 0.3	1.6 ± 0.4
11:00	1.7 ± 0.7	0.9 ± 0.3	0.9 ± 0.3	0.8 ± 0.3	0.8 ± 0.3
12:00	2.1 ± 0.8	1.1 ± 0.5	1.4 ± 0.5	1.1 ± 0.4	0.8 ± 0.4
13:00	2.5 ± 0.9	2.2 ± 0.8	1.5 ± 0.6	1.2 ± 0.6	1.0 ± 0.5
14:00	2.3 ± 0.9	1.5 ± 0.6	1.7 ± 0.7	2.0 ± 0.8	2.2 ± 0.6
15:00	3.2 ± 0.9	1.3 ± 0.5	2.0 ± 0.9	2.1 ± 1.0	1.8 ± 0.6
16:00	2.9 ± 0.8	1.2 ± 0.5	2.0 ± 0.8	2.4 ± 1.0	1.5 ± 0.6
17:00	N/A	N/A	2.1 ± 0.9	3.1 ± 0.9	N/A

(Left axis label: Local time [UTC+2])

Figure A4. Average and standard deviation of lidar 10 m wind speed during each release in local time [UTC+2]. Wind data has been resampled to 1 minute intervals.

	Lidar 10 m wind direction [°]				
	16.09.2024	17.09.2024	18.09.2024	19.09.2024	20.09.2024
09:00	N/A	15 ± 40	112 ± 26	153 ± 16	135 ± 78
10:00	N/A	303 ± 32	143 ± 56	93 ± 44	131 ± 24
11:00	113 ± 35	292 ± 68	213 ± 52	122 ± 52	169 ± 61
12:00	139 ± 48	318 ± 63	246 ± 47	172 ± 45	222 ± 50
13:00	315 ± 38	321 ± 42	187 ± 45	236 ± 64	317 ± 55
14:00	319 ± 37	330 ± 44	130 ± 76	55 ± 39	301 ± 12
15:00	317 ± 24	258 ± 43	86 ± 34	57 ± 46	336 ± 44
16:00	329 ± 26	226 ± 39	66 ± 53	72 ± 33	114 ± 43
17:00	N/A	N/A	53 ± 34	73 ± 28	N/A

Local time [UTC+2]

Figure A5. Average and standard deviation of lidar 10 m wind direction during each release in local time [UTC+2]. Wind data has been resampled to 1 minute intervals.
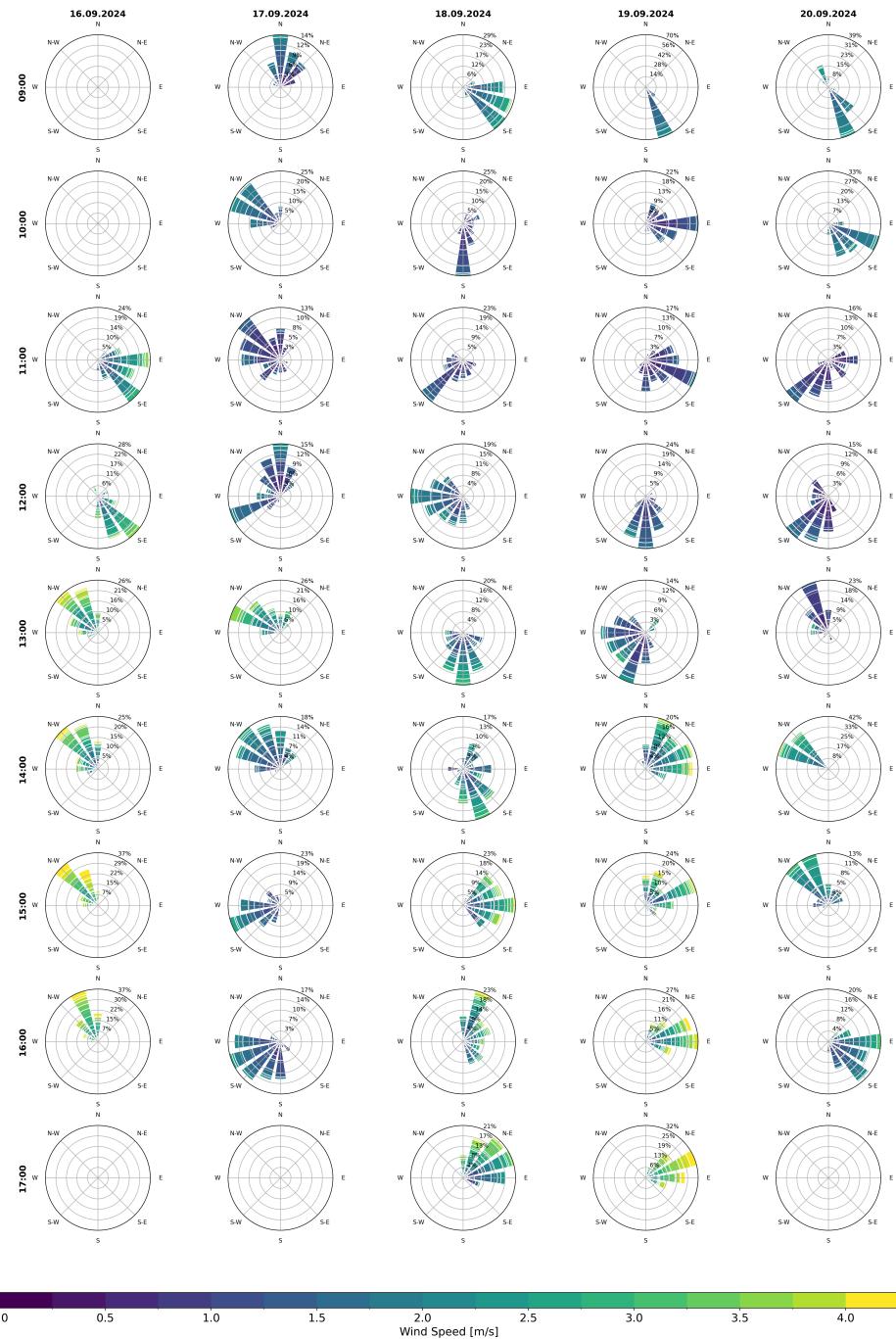
Figure A6. Wind roses of lidar 10 m wind speed and direction during each release in local time [UTC+2].
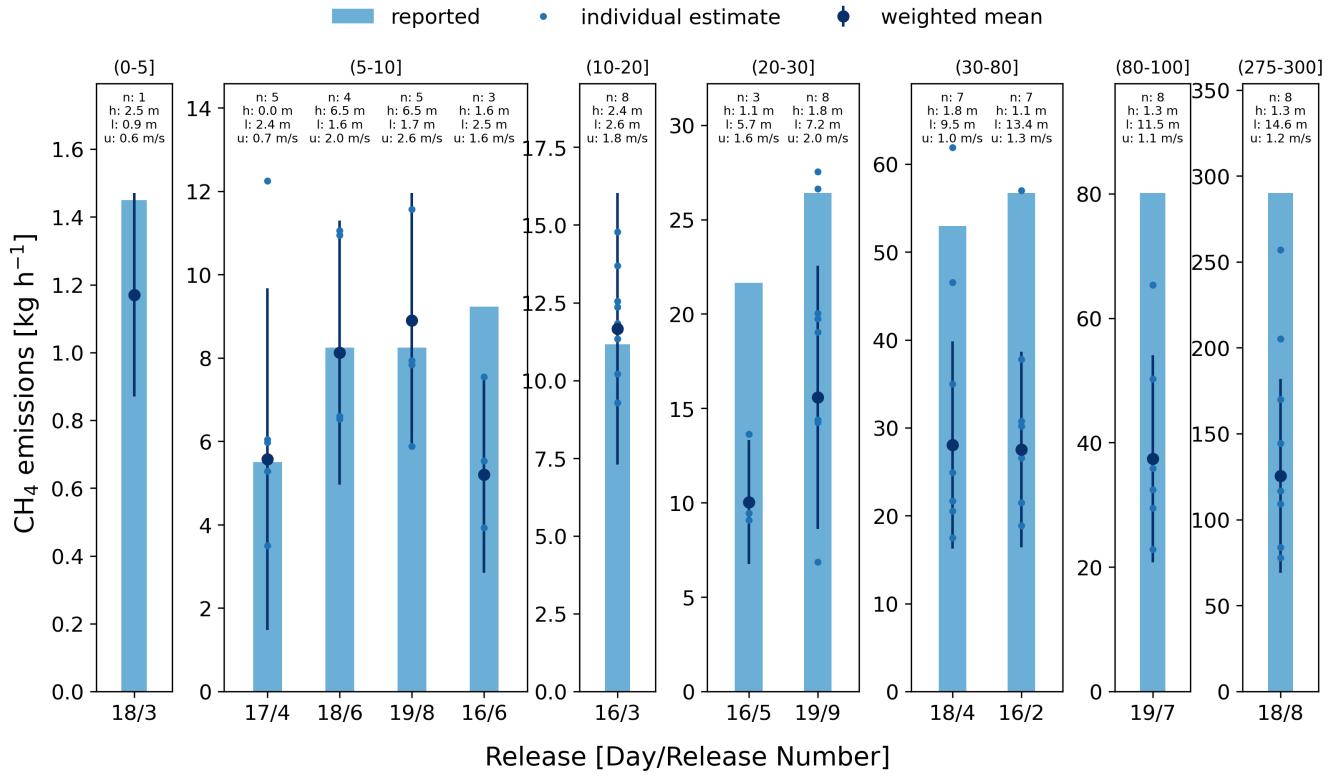
Figure A7. Uncertainty weighted average estimates for each release using U_{eff} derived in this paper. The number of observations n, emission height h, plume length l and average wind speed u are indicated above each bar.

Author contributions. SM conducted the analysis and wrote the paper with input from all co-authors; MV and AH planned and organised the flight campaign and processed the data to georeferenced level 1 data; AM, AB, CJ and VB organised and conducted the controlled release experiment; DB was involved in the planning of the campaign; GK coordinated and supervised the project.

Competing interests. At least one of the (co-)authors is a member of the editorial board of Atmospheric Measurement Techniques.

Acknowledgements. This research has been funded under the framework of UNEP's International Methane Emissions Observatory (IMEO) (agreement no. CCD24-MB7279). Data processing and storage were performed at the Swiss National Supercomputing Centre (CSCS). The AI tools ChatGPT and DeepL were used for grammar checking, copy-editing, and minor wording improvements.

References

Alexe, M., Bergamaschi, P., Segers, A., Detmers, R., Butz, A., Hasekamp, O., Guerlet, S., Parker, R., Boesch, H., Frankenberg, C., Scheepmaker, R. A., Dlugokencky, E., Sweeney, C., Wofsy, S. C., and Kort, E. A.: Inverse modelling of CH4 emissions for 2010–2011 using different satellite retrieval products from GOSAT and SCIAMACHY, Atmos. Chem. Phys., 15, 113–133, https://doi.org/10.5194/acp-15-113-2015, aCP, 2015.

Ayasse, A. K., Cusworth, D., O'Neill, K., Fisk, J., Thorpe, A. K., and Duren, R.: Performance and sensitivity of column-wise and pixel-wise methane retrievals for imaging spectrometers, Atmospheric Measurement Techniques, 16, 6065–6074, https://doi.org/10.5194/amt-16-6065-2023, 2023.

Balcombe, P., Brandon, N., and Hawkes, A.: Characterising the distribution of methane and carbon dioxide emissions from the natural gas supply chain, Journal of Cleaner Production, 172, 2019–2032, https://doi.org/https://doi.org/10.1016/j.jclepro.2017.11.223, 2018.

Borchardt, J., Gerilowski, K., Krautwurst, S., Bovensmann, H., Thorpe, A. K., Thompson, D. R., Frankenberg, C., Miller, C. E., Duren, R. M., and Burrows, J. P.: Detection and quantification of CH_4 plumes using the WFM-DOAS retrieval on AVIRIS-NG hyperspectral data, Atmospheric Measurement Techniques, 14, 1267–1291, https://doi.org/10.5194/amt-14-1267-2021, 2021.

Bousquet, P., Pierangelo, C., Bacour, C., Marshall, J., Peylin, P., Ayar, P. V., Ehret, G., Bréon, F.-M., Chevallier, F., Crevoisier, C., Gibert, F., Rairoux, P., Kiemle, C., Armante, R., Bès, C., Cassé, V., Chinaud, J., Chomette, O., Delahaye, T., Edouart, D., Estève, F., Fix, A., Friker, A., Klonecki, A., Wirth, M., Alpers, M., and Millet, B.: Error Budget of the MEthane Remote LIdar missioN and Its Impact on the Uncertainties of the Global Methane Budget, Journal of Geophysical Research: Atmospheres, 123, 11,766–11,785, https://doi.org/https://doi.org/10.1029/2018JD028907, 2018.

Bruno, J. H., Jervis, D., Varon, D. J., and Jacob, D. J.: U-Plume: automated algorithm for plume detection and source quantification by satellite point-source imagers, Atmospheric Measurement Techniques, 17, 2625–2636, https://doi.org/10.5194/amt-17-2625-2024, 2024.

Conrad, B. M., Tyner, D. R., and Johnson, M. R.: Robust probabilities of detection and quantification uncertainty for aerial methane detection: Examples for three airborne technologies, Remote Sensing of Environment, 288, 113 499, https://doi.org/https://doi.org/10.1016/j.rse.2023.113499, 2023.

Cusworth, D. H., Duren, R. M., Thorpe, A. K., Eastwood, M. L., Green, R. O., Dennison, P. E., Frankenberg, C., Heckler, J. W., Asner, G. P., and Miller, C. E.: Quantifying Global Power Plant Carbon Dioxide Emissions With Imaging Spectroscopy, AGU Advances, 2, e2020AV000 350, https://doi.org/10.1029/2020AV000350, 2021.

Duren, R. M., Thorpe, A. K., Foster, K. T., Rafiq, T., Hopkins, F. M., Yadav, V., Bue, B. D., Thompson, D. R., Conley, S., Colombi, N. K., et al.: California's methane super-emitters, Nature, 575, 180–184, 2019.

Eastwood, M. L., Thompson, D., Green, R. O., Fahlen, J., Adams, T., Brandt, A., Brodrick, P. G., Chlus, A., Kort, E. A., Reuland, F., et al.: Direct Measurement of Plume Velocity to Characterize Point Source Emissions, Authorea Preprints, 2025.

European Parliament and the Council of the European Union: REGULATION (EC) No 166/2006: Establishment of a European Pollutant Release and Transfer Register and amending Council Directives 91/689/EEC and 96/61, 2006.

Fahlen, J. E., Brodrick, P. G., Coleman, R. W., Elder, C. D., Thompson, D. R., Thorpe, A. K., Green, R. O., Green, J. J., Lopez, A. M., and Xiang, C.: Sensitivity and Uncertainty in Matched-Filter-Based Gas Detection With Imaging Spectroscopy, IEEE Transactions on Geoscience and Remote Sensing, 62, 1–10, https://doi.org/10.1109/TGRS.2024.3440174, 2024.

Fleagle, R. G. and Businger, J. A.: An introduction to atmospheric physics, Academic Press, https://doi.org/https://doi.org/10.1016/S0074-6142(08)60498-2, 1980.

Foote, M. D., Dennison, P. E., Thorpe, A. K., Thompson, D. R., Jongaramrungruang, S., Frankenberg, C., and Joshi, S. C.: Fast and accurate retrieval of methane concentration from imaging spectrometer data using sparsity prior, IEEE Transactions on Geoscience and Remote Sensing, 58, 6480–6492, 2020.

Fraser, A., Palmer, P. I., Feng, L., Boesch, H., Cogan, A., Parker, R., Dlugokencky, E. J., Fraser, P. J., Krummel, P. B., Langenfelds, R. L., O'Doherty, S., Prinn, R. G., Steele, L. P., Van Der Schoot, M., and Weiss, R. F.: Estimating regional methane surface fluxes: the relative importance of surface and GOSAT mole fraction measurements, Atmospheric Chemistry and Physics, 13, 5697–5713, https://doi.org/10.5194/acp-13-5697-2013, 2013.

Gorroño, J., Varon, D. J., Irakulis-Loitxate, I., and Guanter, L.: Understanding the potential of Sentinel-2 for monitoring methane point emissions, Atmospheric Measurement Techniques, 16, 89–107, https://doi.org/10.5194/amt-16-89-2023, 2023.

Gorroño, J., Pei, Z., Valverde, A., and Guanter, L.: Considering the observation and illumination angular configuration for an improved detection and quantification of methane emissions, EGUsphere, 2025, 1–19, https://doi.org/10.5194/egusphere-2025-4924, 2025.

Green, R. O., Schaepman, M. E., Mouroulis, P., Geier, S., Shaw, L., Hueini, A., Bernas, M., McKinley, I., Smith, C., Wehbe, R., Eastwood, M., Vinckier, Q., Liggett, E., Zandbergen, S., Thompson, D., Sullivan, P., Sarture, C., Van Gorp, B., and Helm-linger, M.: Airborne Visible/Infrared Imaging Spectrometer 3 (AVIRIS-3), in: 2022 IEEE Aerospace Conference (AERO), pp. 1–10, https://doi.org/10.1109/AERO53065.2022.9843565, 2022.

Guanter, L., Irakulis-Loitxate, I., Gorroño, J., Sánchez-García, E., Cusworth, D. H., Varon, D. J., Cogliati, S., and Colombo, R.: Mapping methane point emissions with the PRISMA spaceborne imaging spectrometer, Remote Sensing of Environment, 265, 112 671, https://doi.org/https://doi.org/10.1016/j.rse.2021.112671, 2021.

Guanter, L., Warren, J., Omara, M., Chulakadabba, A., Roger, J., Sargent, M., Franklin, J. E., Wofsy, S. C., and Gautam, R.: Detection and quantification of methane plumes with the MethaneAIR airborne spectrometer, Atmospheric Measurement Techniques, 18, 3857–3872, https://doi.org/10.5194/amt-18-3857-2025, 2025.

Hersbach, H., Bell, B., Berrisford, P., Biavati, G., Horányi, A., Muñoz Sabater, J., Nicolas, J., Peubey, C., Radu, R., Rozum, I., Schepers, D., Simmons, A., Soci, C., Dee, D., and Thépaut, J.-N.: ERA5 hourly data on single levels from 1940 to present, Copernicus Climate Change Service (C3S) Climate Data Store (CDS), https://doi.org/10.24381/cds.adbb2d47, 2018.

Hueni, A., Geier, S., Vögtli, M., LaHaye, J., Rosset, J., Berger, D., Sierro, L. J., Jospin, L. V., Thompson, D. R., Schläpfer, D., Green, R. O., Loeliger, T., Skaloud, J., and Schaepman, M. E.: The AVIRIS-4 Airborne Imaging Spectrometer, IEEE Geoscience and Remote Sensing Letters, 22, 1–5, https://doi.org/10.1109/LGRS.2025.3572349, 2025.

IGN: RGE ALTI® v2.0: Digital Elevation Model (DEM) of France, https://geoservices.ign.fr/documentation/donnees/alti/rgealti, 2018.

Jacob, D. J., Varon, D. J., Cusworth, D. H., Dennison, P. E., Frankenberg, C., Gautam, R., Guanter, L., Kelley, J., McKeever, J., Ott, L. E., Poulter, B., Qu, Z., Thorpe, A. K., Worden, J. R., and Duren, R. M.: Quantifying methane emissions from the global scale down to point sources using satellite observations of atmospheric methane, Atmos. Chem. Phys., 22, 9617–9646, https://doi.org/10.5194/acp-22-9617-2022, aCP, 2022.

Jongaramrungruang, S., Thorpe, A. K., Matheou, G., and Frankenberg, C.: MethaNet – An AI-driven approach to quantifying methane point-source emission from high-resolution 2-D plume imagery, Remote Sensing of Environment, 269, 112 809, https://doi.org/10.1016/j.rse.2021.112809, 2022.

Joyce, P., Ruiz Villena, C., Huang, Y., Webb, A., Gloor, M., Wagner, F. H., Chipperfield, M. P., Barrio Guilló, R., Wilson, C., and Boesch, H.: Using a deep neural network to detect methane point sources and quantify emissions from PRISMA hyperspectral satellite images, Atmospheric Measurement Techniques, 16, 2627–2640, https://doi.org/10.5194/amt-16-2627-2023, 2023.

Krautwurst, S., Fruck, C., Wolff, S., Borchardt, J., Huhs, O., Gerilowski, K., Gałkowski, M., Kiemle, C., Quatrevalet, M., Wirth, M., Mallaun, C., Burrows, J. P., Gerbig, C., Fix, A., Bösch, H., and Bovensmann, H.: Identification and Quantification of CH_4 Emissions from Madrid Landfills using Airborne Imaging Spectrometry and Greenhouse Gas Lidar, EGUsphere, 2024, 1–52, https://doi.org/10.5194/egusphere-2024-3182, 2024.

Kuhlmann, G., Koene, E. F. M., Meier, S., Santaren, D., Broquet, G., Chevallier, F., Hakkarainen, J., Nurmela, J., Amorós, L., Tamminen, J., and Brunner, D.: The ddeq Python library for point source quantification from remote sensing images (Version 1.0), accepted in Geo. Mod. Dev., https://doi.org/10.5194/egusphere-2023-2936, 2024.

Kuhlmann, G., Stavropoulou, F., Schwietzke, S., Zavala-Araiza, D., Thorpe, A., Hueni, A., Emmenegger, L., Calcan, A., Röckmann, T., and Brunner, D.: Evidence of successful methane mitigation in one of Europe's most important oil production region, Atmospheric Chemistry and Physics, 25, 5371–5385, https://doi.org/10.5194/acp-25-5371-2025, 2025.

McManemin, A.: Controlled release testing of multiple European methane measurement technologies, Master's thesis, Stanford University, https://doi.org/10.25740/jk575gf5993, stanford Digital Repository, 2025.

Ouerghi, E., Ehret, T., Facciolo, G., Meinhardt, E., Marion, R., and Morel, J.-M.: Tightening up methane plume source rate estimation in EnMAP and PRISMA images, Atmospheric Measurement Techniques, 18, 4611–4629, https://doi.org/10.5194/amt-18-4611-2025, 2025.

Pei, Z., Han, G., Mao, H., Chen, C., Shi, T., Yang, K., Ma, X., and Gong, W.: Improving quantification of methane point source emissions from imaging spectroscopy, Remote Sensing of Environment, 295, 113 652, https://doi.org/https://doi.org/10.1016/j.rse.2023.113652, 2023.

Plewa, T., Butz, A., Frankenberg, C., Thorpe, A. K., and Marshall, J.: Improvements of AI-driven emission estimation for point sources applied to high resolution 2-D methane-plume imagery, Remote Sensing of Environment, 331, 115 002, https://doi.org/https://doi.org/10.1016/j.rse.2025.115002, 2025.

Rouet-Leduc, B. and Hulbert, C.: Automatic detection of methane emissions in multispectral satellite imagery using a vision transformer, Nature Communications, 15, 3801, 2024.

Sánchez-García, E., Gorroño, J., Irakulis-Loitxate, I., Varon, D. J., and Guanter, L.: Mapping methane plumes at very high spatial resolution with the WorldView-3 satellite, Atmospheric Measurement Techniques, 15, 1657–1674, https://doi.org/10.5194/amt-15-1657-2022, 2022.

Saunois, M., Stavert, A. R., Poulter, B., Bousquet, P., Canadell, J. G., Jackson, R. B., Raymond, P. A., Dlugokencky, E. J., Houweling, S., Patra, P. K., Ciais, P., Arora, V. K., Bastviken, D., Bergamaschi, P., Blake, D. R., Brailsford, G., Bruhwiler, L., Carlson, K. M., Carrol, M., Castaldi, S., Chandra, N., Crevoisier, C., Crill, P. M., Covey, K., Curry, C. L., Etiope, G., Frankenberg, C., Gedney, N., Hegglin, M. I., Höglund-Isaksson, L., Hugelius, G., Ishizawa, M., Ito, A., Janssens-Maenhout, G., Jensen, K. M., Joos, F., Kleinen, T., Krummel, P. B., Langenfelds, R. L., Laruelle, G. G., Liu, L., Machida, T., Maksyutov, S., McDonald, K. C., McNorton, J., Miller, P. A., Melton, J. R., Morino, I., Müller, J., Murguia-Flores, F., Naik, V., Niwa, Y., Noce, S., O'Doherty, S., Parker, R. J., Peng, C., Peng, S., Peters, G. P., Prigent, C., Prinn, R., Ramonet, M., Regnier, P., Riley, W. J., Rosentreter, J. A., Segers, A., Simpson, I. J., Shi, H., Smith, S. J., Steele, L. P., Thornton, B. F., Tian, H., Tohjima, Y., Tubiello, F. N., Tsuruta, A., Viovy, N., Voulgarakis, A., Weber, T. S., Van Weele, M., Van Der Werf, G. R., Weiss, R. F., Worthy, D., Wunch, D., Yin, Y., Yoshida, Y., Zhang, W., Zhang, Z., Zhao, Y., Zheng, B., Zhu, Q., Zhu, Q., and Zhuang, Q.: The Global Methane Budget 2000–2017, Earth System Science Data, 12, 1561–1623, https://doi.org/10.5194/essd-12-1561-2020, 2020.

Schaum, A.: A uniformly most powerful detector of gas plumes against a cluttered background, Remote Sensing of Environment, 260, 112 443, https://doi.org/https://doi.org/10.1016/j.rse.2021.112443, 2021.

Schläpfer, D. and Richter, R.: Geo-atmospheric processing of airborne imaging spectrometry data. Part 1: Parametric orthorectification, International Journal of Remote Sensing, 23, 2609–2630, https://doi.org/10.1080/01431160110115825, 2002.

Schläpfer, D., Hueni, A., and Richter, R.: Cast Shadow Detection to Quantify the Aerosol Optical Thickness for Atmospheric Correction of High Spatial Resolution Optical Imagery, Remote Sensing, 10, https://doi.org/10.3390/rs10020200, 2018.

Schwaerzel, M., Emde, C., Brunner, D., Morales, R., Wagner, T., Berne, A., Buchmann, B., and Kuhlmann, G.: Three-dimensional radiative transfer effects on airborne and ground-based trace gas remote sensing, Atmospheric Measurement Techniques, 13, 4277–4293, https://doi.org/10.5194/amt-13-4277-2020, 2020.

Seinfeld, J. H. and Pandis, S. N.: Atmospheric chemistry and physics: from air pollution to climate change, John Wiley & Sons, 2016.

Shaw, L. A., Geier, S., Mckinley, I. M., Bernas, M. A., Gharakhanian, M., Dergevorkian, A., Eastwood, M. L., Mouroulis, P., and Green, R. O.: Design, alignment, and laboratory calibration of the compact wide swath imaging spectrometer II (CWIS-II), in: Imaging Spectrometry XXV: Applications, Sensors, and Processing, vol. 12235, p. 1223502, SPIE, 2022.

Stavropoulou, F., Vinković, K., Kers, B., de Vries, M., van Heuven, S., Korbeń, P., Schmidt, M., Wietzel, J., Jagoda, P., Necki, J. M., Bartyzel, J., Maazallahi, H., Menoud, M., van der Veen, C., Walter, S., Tuzson, B., Ravelid, J., Morales, R. P., Emmenegger, L., Brunner, D., Steiner, M., Hensen, A., Velzeboer, I., van den Bulk, P., Denier van der Gon, H., Delre, A., Edjabou, M. E., Scheutz, C., Corbu, M., Iancu, S., Moaca, D., Scarlat, A., Tudor, A., Vizireanu, I., Calcan, A., Ardelean, M., Ghemulet, S., Pana, A., Constantinescu, A., Cusa, L., Nica, A., Baciu, C., Pop, C., Radovici, A., Mereuta, A., Stefanie, H., Dandocsi, A., Hermans, B., Schwietzke, S., Zavala-Araiza, D., Chen, H., and Röckmann, T.: High potential for CH_4 emission mitigation from oil infrastructure in one of EU's major production regions, Atmospheric Chemistry and Physics, 23, 10 399–10 412, https://doi.org/10.5194/acp-23-10399-2023, 2023.

Thompson, D. R., Leifer, I., Bovensmann, H., Eastwood, M., Fladeland, M., Frankenberg, C., Gerilowski, K., Green, R. O., Kratwurst, S., Krings, T., Luna, B., and Thorpe, A. K.: Real-time remote detection and measurement for airborne imaging spectroscopy: a case study with methane, Atmospheric Measurement Techniques, 8, 4383–4397, https://doi.org/10.5194/amt-8-4383-2015, 2015.

Thorpe, A., Frankenberg, C., Aubrey, A., Roberts, D., Nottrott, A., Rahn, T., Sauer, J., Dubey, M., Costigan, K., Arata, C., Steffke, A., Hills, S., Haselwimmer, C., Charlesworth, D., Funk, C., Green, R., Lundeen, S., Boardman, J., Eastwood, M., Sarture, C., Nolte, S., Mccubbin, I., Thompson, D., and McFadden, J.: Mapping methane concentrations from a controlled release experiment using the next generation airborne visible/infrared imaging spectrometer (AVIRIS-NG), Remote Sensing of Environment, 179, 104–115, https://doi.org/https://doi.org/10.1016/j.rse.2016.03.032, 2016.

Thorpe, A. K., O'Handley, C., Emmitt, G. D., DeCola, P. L., Hopkins, F. M., Yadav, V., Guha, A., Newman, S., Herner, J. D., Falk, M., and Duren, R. M.: Improved methane emission estimates using AVIRIS-NG and an Airborne Doppler Wind Lidar, Remote Sensing of Environment, 266, 112 681, https://doi.org/https://doi.org/10.1016/j.rse.2021.112681, 2021.

Varon, D. J., Jacob, D. J., McKeever, J., Jervis, D., Durak, B. O. A., Xia, Y., and Huang, Y.: Quantifying methane point sources from fine-scale satellite observations of atmospheric methane plumes, Atmospheric Measurement Techniques, 11, 5673–5686, https://doi.org/10.5194/amt-11-5673-2018, 2018.

Williams, J. P., Omara, M., Himmelberger, A., Zavala-Araiza, D., MacKay, K., Benmergui, J., Sargent, M., Wofsy, S. C., Hamburg, S. P., and Gautam, R.: Small emission sources in aggregate disproportionately account for a large majority of total methane emissions from the US oil and gas sector, Atmospheric Chemistry and Physics, 25, 1513–1532, https://doi.org/10.5194/acp-25-1513-2025, 2025.

Zavala-Araiza, D., Lyon, D., Alvarez, R. A., Palacios, V., Harriss, R., Lan, X., Talbot, R., and Hamburg, S. P.: Toward a Functional Definition of Methane Super-Emitters: Application to Natural Gas Production Sites, Environmental Science & Technology, 49, 8167–8174, https://doi.org/10.1021/acs.est.5b00133, pMID: 26148555, 2015.

Zhang, S., Ma, J., Zhang, X., and Guo, C.: Atmospheric remote sensing for anthropogenic methane emissions: Applications and research opportunities, Science of The Total Environment, 893, 164 701, 2023.